2017

Experimental and Numerical Investigation of Pressure Drop in Silicon Carbide Fuel Rod for Application in Pressurized Water Reactors

Ahmed Musafi Abir
University of South Carolina

EXPERIMENTAL AND NUMERICAL INVESTIGATION OF PRESSURE DROP IN SILICON CARBIDE FUEL ROD FOR APPLICATION IN PRESSURIZED WATER REACTORS

by

Ahmed Musafi Abir

Bachelor of Science
Bangladesh University of Engineering and Technology, 2013

Submitted in Partial Fulfillment of the Requirements

For the Degree of Master of Science in

Mechanical Engineering

College of Engineering and Computing

University of South Carolina

2017

Accepted by:

Jamil A. Khan, Director of Thesis

Tanvir I. Farouk, Reader

Titan C. Paul, Reader

Cheryl L. Addy, Vice Provost and Dean of the Graduate School

ACKNOWLEDGEMENTS

I would like to express my deep gratitude and thanks to my advisor Dr. Jamil Khan, for his continuous guidance, support, invaluable suggestions and sharing his knowledge throughout my Masters study. It has been a great privilege and honor for me to work with him.

I would also like to thank Dr. Leo A. Carrilho from the Westinghouse Company for his invaluable suggestions and assistance. I also thank Dr. Tanvir I. Farouk and Dr. Titan C. Paul for officially agreeing to serve as a reader, and for their advice during my research.

Special thanks to graduate friends, Rajib Mahamud, Azzam Salman, Saad Oudah, Noble Anumbe, Nabeel Abdulrazzaq, Amitav Tikadar, Abdulwahab Alhashem and Bill Bradley for their suggestions and help.

Finally I would like to thank the Westinghouse Company for funding this research.

ABSTRACT

Spacer grids are used in pressurized water reactors (PWRs) fuel assemblies which enhances heat transfer from fuel rods. However, there remain regions of low turbulence in between the spacer grids which contributes to lower heat transfer. To enhance turbulence in these regions surface roughness is applied on the fuel rod walls. Meyer et al [1] used empirical correlations to predict heat transfer and friction factor for artificially roughened fuel rod bundles at high performance light water reactors (LWRs). At present, several types of materials are being used for fuel rod cladding including zircaloy, uranium oxide, etc. But researchers are actively searching for new material that can be a more practical alternative. Silicon carbide (SiC) has been identified as a material of interest for application as fuel rod cladding [2].

The current study deals with the experimental investigation to find out the friction factor increase of a SiC fuel rod with 3D surface roughness. The SiC rod was tested at USC's Single Heater Element Loop Tester (SHELT) loop. The experiment was conducted in turbulent flowing Deionized (DI) water at steady state conditions. Measurements of flow rate and pressure drop were made. The experimental results were also validated by Computational Fluid Dynamics (CFD) analysis in ANSYS Fluent. To simplify the CFD analysis and to save computational resources the 3D roughness was approximated as a 2D one. The friction factor results of the CFD investigation was found to lie within ±8% of the experimental results. Simulations were also conducted with the energy equation turned on,

and a heat generation of 8 kW applied to the rod. A maximum heat transfer enhancement of 18.4% was achieved at the highest flow rate investigated (i.e. Re=109204).

TABLE OF CONTENTS

LIST OF TABLES

LIST OF FIGURES

LIST OF SYMBOLS

U_m	Mean Velocity.
Q	Flow Rate.
A_c	Cross Sectional Area of test section.
r_o	Outer Diameter of the test section.
r_i	Diameter of the nuclear fuel rod
Re	Reynolds Number.
D_h	Hydraulic Diameter of the test section.
ϑ	Kinematic viscosity of DI water.
f	Friction factor.
Δp	Differential Pressure Drop.
Δx	Length.
Re	Reynolds Number.
ρ	Density of DI water.
k_s	Sand grain roughness height.
C_f	Skin friction coefficient.
U_τ	Wall friction velocity.
y^+	Non-dimensional wall distance
T_{b_1}	Bulk temperature at the entrance of rough section.
T_{b_2}	Bulk temperature at the outlet of the rough section.

h Heat transfer coefficient.

k_f conductivity of DI water.

Nu Nusselt Number.

P Prandtl Number.

q'' Heat flux per unit area.

h Heat transfer coefficient.

T_w Temperature at wall.

Nu Nusselt Number.

q'' Heat flux per unit area

LIST OF ABBREVIATIONS

CFD ..... Computational Fluid Dynamics

CVI ..... Chemical Vapor Infiltration

DI ..... Deionized

LOCA ..... Loss of Coolant Accidents

PWR ..... Pressurized Water Reactor

RANS ..... Reynolds Averaged Navier-Stoke

SiC ..... Silicon Carbide

SST ..... Shear Stress Transport

UO_2 ..... Uranium Dioxide

Zr ..... Zirconium

CHAPTER 1

INTRODUCTION

Turbulence is used as a tool to enhance heat transfer from fuel rods in Pressurized Water Reactors (PWR) fuel rod assemblies. For this purpose, spacer grids are used in the fuel assemblies. Unfortunately, these only produce a localized turbulence thus the turbulence along the fuel rod is low. Thus, to enhance the turbulence along the entire length of the rods different types of surface roughness are used.

Investigators have reported significant improvements in heat transfer by employing the artificial roughening technique, mainly on surface of circular channels [3]. Structured artificial roughness acts as a boundary layer disturber in the near-wall turbulent flow structure to promote higher momentum and heat transport along the surface.

Zirconium (Zr)-based alloys are used universally in water-cooled reactors as cladding for nuclear fuel. Zirconium-based alloy cladding prevents release of fission products into the coolant but introduces some limitations to the nuclear reactors design. These limits are mainly due to Zirconium-based alloy embrittlement through chemical and radiation damage, early pellet-cladding mechanical interaction, and restricted mechanical performance and chemical stability at elevated temperature.

Unfortunately use of surface roughening of fuel rods for heat transfer enhancement has its drawbacks. The surface roughness causes significant rise in the friction factor, which means that higher pumping costs will be involved. Thus, researchers and scientists are continuously struggling to come up with surface roughness that will be the most practical

and economic for use in PWR fuel rod assemblies. The purpose of the current investigation is to experimentally quantify the friction factor for a proposed SiC fuel rod with artificial roughness, and a consequent CFD analysis for validation of the results. And then CFD model will be used to approximate heat transfer enhancement for the roughness design.

SiC clad fuel rods have been identified as a suitable replacement for the Zr alloys for a number of their beneficial properties such as lower thermal neutron absorption [4], corrosion resistance and resistance to hydrogen embrittlement [5], projected stable response to beyond design basis accidents, such as station blackout accidents approaching 2000 ˚C [6], and stable response to design basis loss of coolant accidents (LOCA). However the SiC is a ceramic and it exhibits relatively brittle behaviour compared to the dilute Zr alloy. To enhance mechnaical properties of SiC it can be fabricated into composite tubes. Tube samples formed into composites were tested using 4-point flexure and instrumented impact at room temperature and it was found to enhance the strength and strain properties of SiC [2]. Another undesirable property of the SiC when compared with the Zr alloy is that it has a lower conductivity. Thus before the SiC rod is introduced into reactor cores it should be subjected to careful evaluation.

CHAPTER 2

BACKGROUND REVIEW

With the global rise in energy demand and its scarcity researchers around the globe are trying hard to figure out ways to make energy efficient systems. The effect of surface roughness on pressure drop has been an area of interest for eminent researches for a very long time. An increase in roughness increases the friction factor. Nikuradse conducted the classical series of experiments with pipes roughened by sand grains [7]. He studied the law of resistance in the Reynolds number range of 10^4 to 10^6 for pipes with circular cross section and different degrees of roughness defined by $\frac{k}{r}$ (where k is average projection of the roughness and r is the radius of pipe). In order to define the law of resistance he divided the flow conditions into three ranges. In range I for small Reynold No. the resistance factor is the same for rough and for smooth pipes. In this region the projection of the sand grain roughness lie totally within the laminar layer. In range II an increase in the resistance factor was observed for increasing Reynolds number. The thickness of the laminar layer is same as that of the projections in this range. For the range III the resistance factor is independent of the Reynolds number . Here all projections of the roughening extend through the laminar layer. Therefore, he found that the flow resistance in the laminar region was not effected by the roughness height. However in the transition and turbulent flow region an increase in flow resistance occurs due to sand grains extending out of the laminar sublayer into the turbulent region, and production of vortices.

Mark Steinke and Satish Kandilkar [8] suggested heat transfer enhancement techniques in single phase flows which include: flow transition, breakup of boundary layer, entrance region, vibration, electric fields, swirl flow and mixers. R.J. Firth and L. Meyer [9] conducted heat transfer and friction factor performance studies in four different types of artificially roughnened surfaces:

1. Square transverse ribbed
2. Helically ribbed
3. Trapezoidal transverse ribbed
4. Three dimensional surfaces

These surfaces were developed as part of the nuclear reactor programmes with the objective of improving the rate of heat removal from fuel pins in gas cooled reactors. The friction factor and the heat transfer studies were conducted under fully turbulent flows of Reynolds numbers upto 10^6. The study concluded that the three dimensional surface has the best overall thermal performance which showed a thermal preformance improvement of 15% compared with the trapezoidal transverse ribbed surface. However the 3D surface has the disadvantage that the surface is more sensitive to changes in the surface geometry. For the transverse trapezoidal roughness there is no advantage. If a roughness is needed with a low friction factor without a reduction in rib height then the best alternate is the helically ribbed surface. The square transverse ribbed surface has an overall performance that compares well with the other surfaces, and the helically ribbed surfaces has a thermal performance which compares closely with the square ribbed surface.

Li et al [10] experimentally investigated by measuring the heat transfer in two-dimensional roughness tubes with different roughness heights at various Reynolds

numbers. They concluded that there is a maximum Nusselt number ratio for fixed roughness height with increasing Reynolds number. They concluded that when the roughness height is more than five times of the viscous sublayer thickness, the flow friction begins to increase sharply but heat transfer is slowly enhanced. They concluded that the best heat transfer enhancement for a given pumping power is reached when roughness height is three times of viscous sub layer thickness.

Ryu et al [11] conducted a computational investigation of turbulent flow in channels with two-dimensional ribs and three-dimensional blocks. Reynolds-averaged Navier-Stokes (RANS) equations, coupled with k-ω turbulence model with near-wall treatment were solved by a finite-volume method. For the two-dimensional rib roughened channels they conducted a study on four different types of ribs: square ribs, triangular ribs, semicircular ribs, wavy wall. It was concluded from that study that the square ribs exert the most resistance among the four shapes considered while wavy wall offers the least. An extension of this work [12] presented the heat transfer characteristics of turbulent flow in channels with two-dimensional ribs and three-dimensional blocks. They concluded that the heat transfer enhancement corresponds to the maximum resistance coefficient for two-dimensional ribs. The maximum heat transfer is achieved for the square rib, and it decreases as the shape changes to triangular, to semicircular and to wavy wall.

Carrilho et al [13] conducted a heat transfer and flow resistance study, by both experimentation and computatoion due to square transverse ribbed surface on a single fuel rod. His experimental and computational results suggested a heat transfer enhancement of 50%. Umair et al [14] conducted a similar study due to three dimensional diamond shaped blocks in turbulent flow. He recorded a maximum heat transfer enhancement of 83%.

CHAPTER 3

EXPERIMENTAL SETUP

3.1 Single Heater Element Loop Tester Loop (SHELT)

SHELT is a thermal hydraulic closed loop designed for vertical flow testing, which is utilized to measure the convective heat transfer and friction factors at single tube surfaces representative of those used in commercial nuclear PWRs. The SHELT loop piping is constructed from 48.3 mm diameter, 3.68 mm thickness, 304 stainless steel, schedule 40s piping, including ball valves, elbows, and tees. The connections with the pump are made from 50.8 mm in/outlet to the piping system by means of 50.8 mm to 38 mm stainless steel reducers. The loop is attached to a board parallel to the wall. There are several advantages using this configuration, e.g. flow stability and reduced vibration of the system as all components are coplanar between them. The acrylic flow housing is attached to the loop using tees and flanges. The flow housing is connected to adjustable steel brackets for structural support. The loop has one bypass: Test section flow rate control bypass. The loop can deliver flow rates between 4-14 m^3/h in the annular test channel and has 50 mm insulation on it to reduce heat loss and improve energy balance. The facility can withstand maximum pressures of 1 MPa and temperatures of up to 200˚C. A schematic of the loop is presented in Figure 3.1 and the actual loop is shown in Figure 3.2. The major components of the loop are as follows:

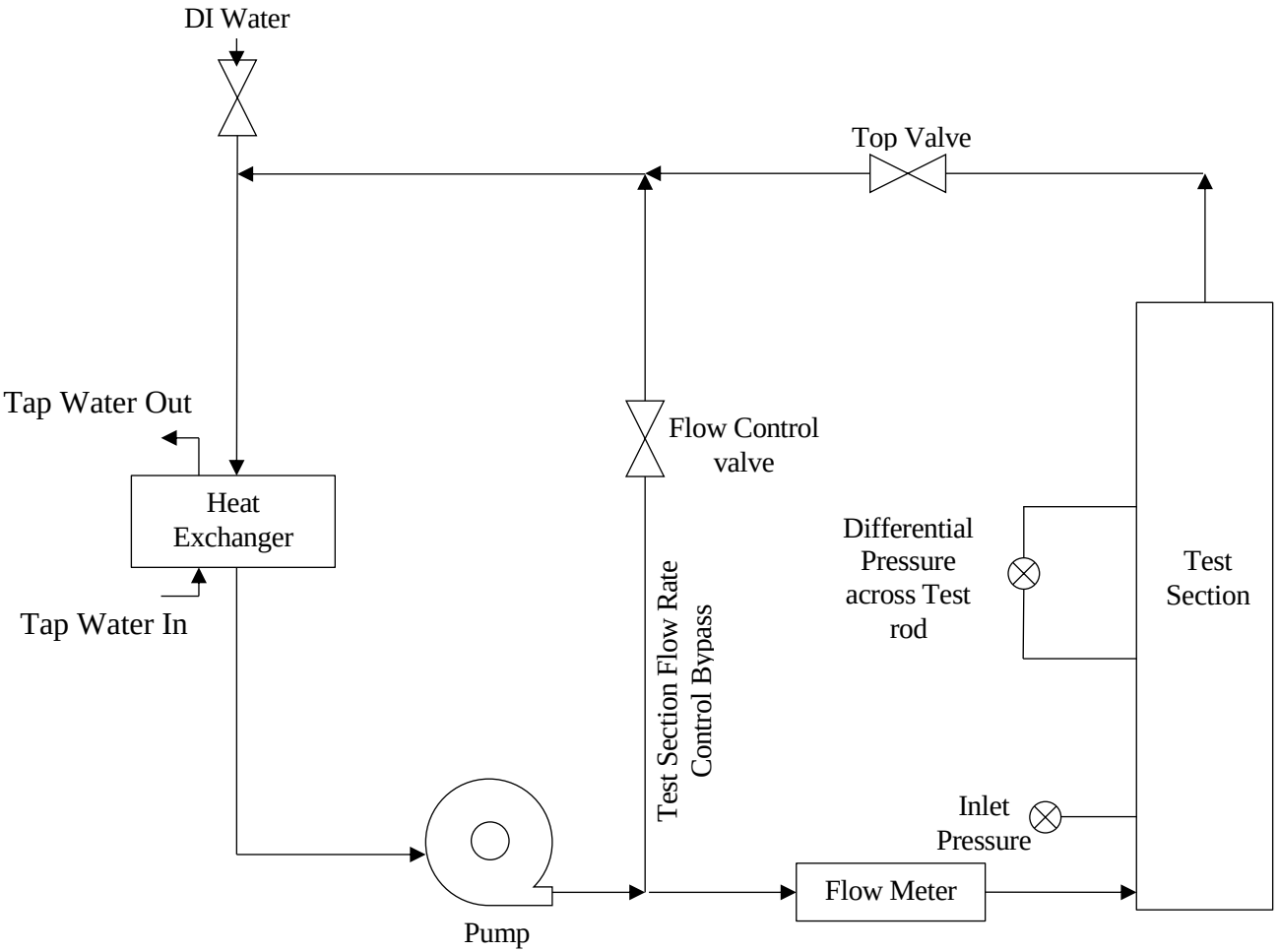

Figure 3.1 Schematic of the SHELT Loop

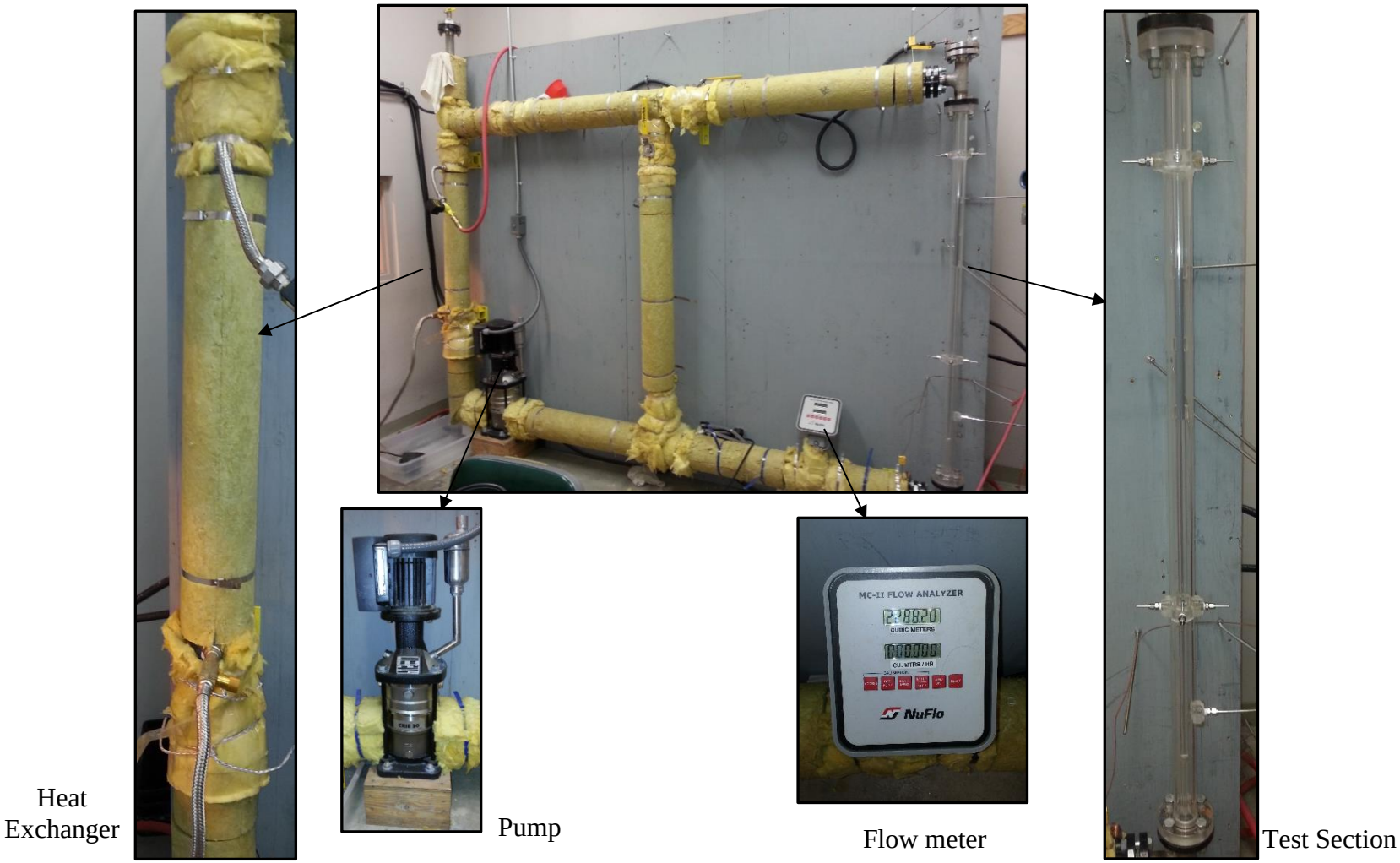

Figure 3.2 The SHELT Loop at USC

3.2 Test Section

The test section (Figure 3.3) consists of two (2) major components: the single simulated fuel rod (Figure 3.4) and the flow housing (Figure 3.5). Specific requirements of the test section include: 0.2 MPa maximum pressure; 50°C maximum temperature. The test section performs the following functions: providing the inlet and outlet to the single simulated fuel rod, providing pressure instrumentation to the heater rods and working fluid (DI water). The cross section of the test section is shown in Figure 3.6.

3.2.1 Single Simulated Fuel Rod

The single simulated fuel rod has three major parts: the top plastic rod, the middle test rod section, and the bottom plastic rod. The single simulated fuel rod is designed such that all the parts components are assembled in line and joined together to form a single rod.

The top plastic rod is 648 mm in length and has outer diameter of 13.8 mm. The test rod (SiC fuel rod) is 266.7 mm in length and has an inner diameter of 8.1 mm and an outer diameter of 13.8 mm. This test rod is attached to the top and bottom plastic rods by press fittings. The bottom plastic rod of 1168.4 mm length and 13.8 mm outer diameter serves the purpose of: supporting the middle test rod section and holding it to the desired elevation from the inlet tee.

3.2.2 Flow Housing

The flow housing provides the appropriate cross section to accommodate the single simulated fuel rod at its center. It has two (2) components: (1) the flow shroud tube and (2) two sets of rod support for ensuring proper alignment.

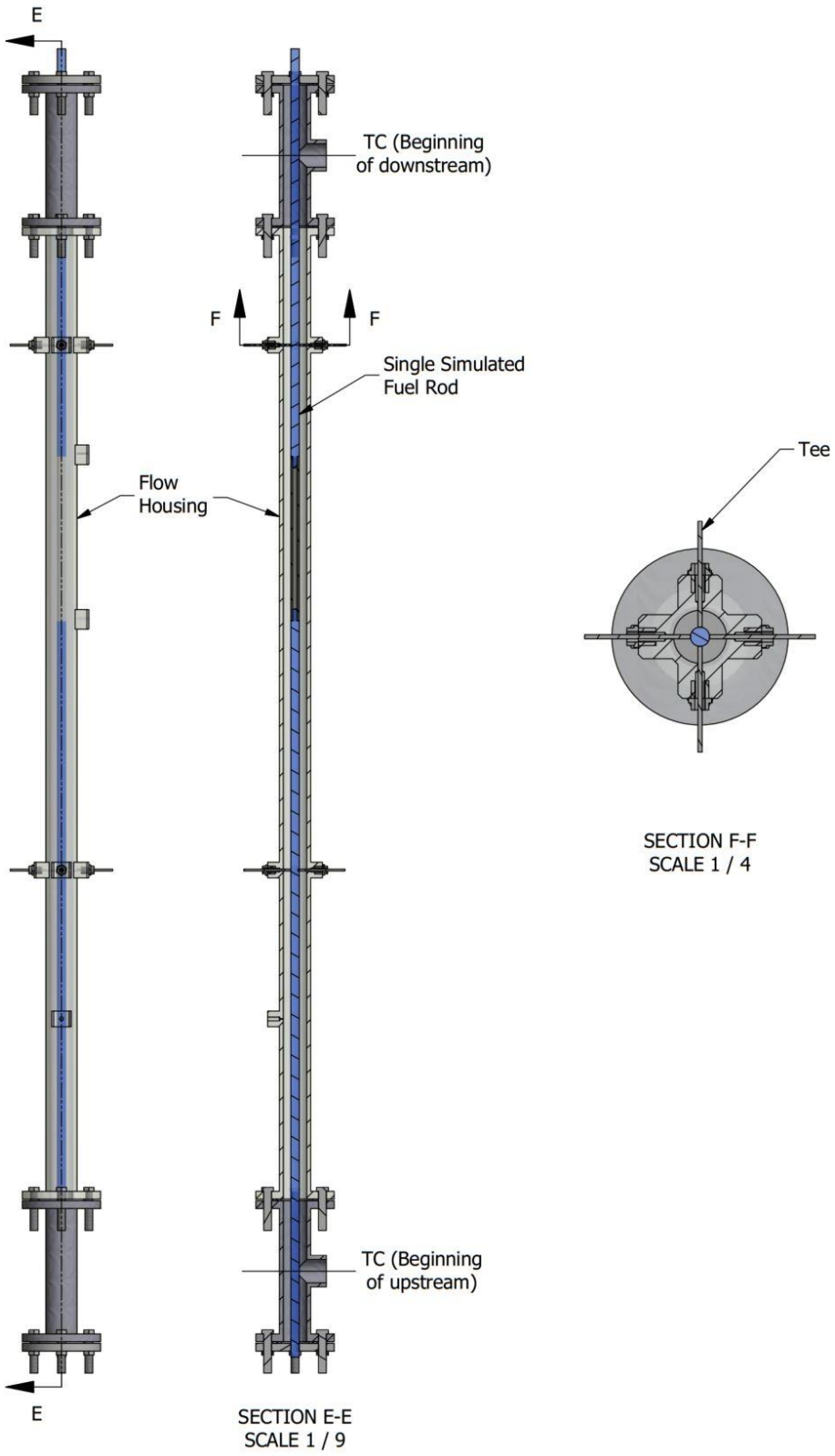

Figure 3.3 Test Section

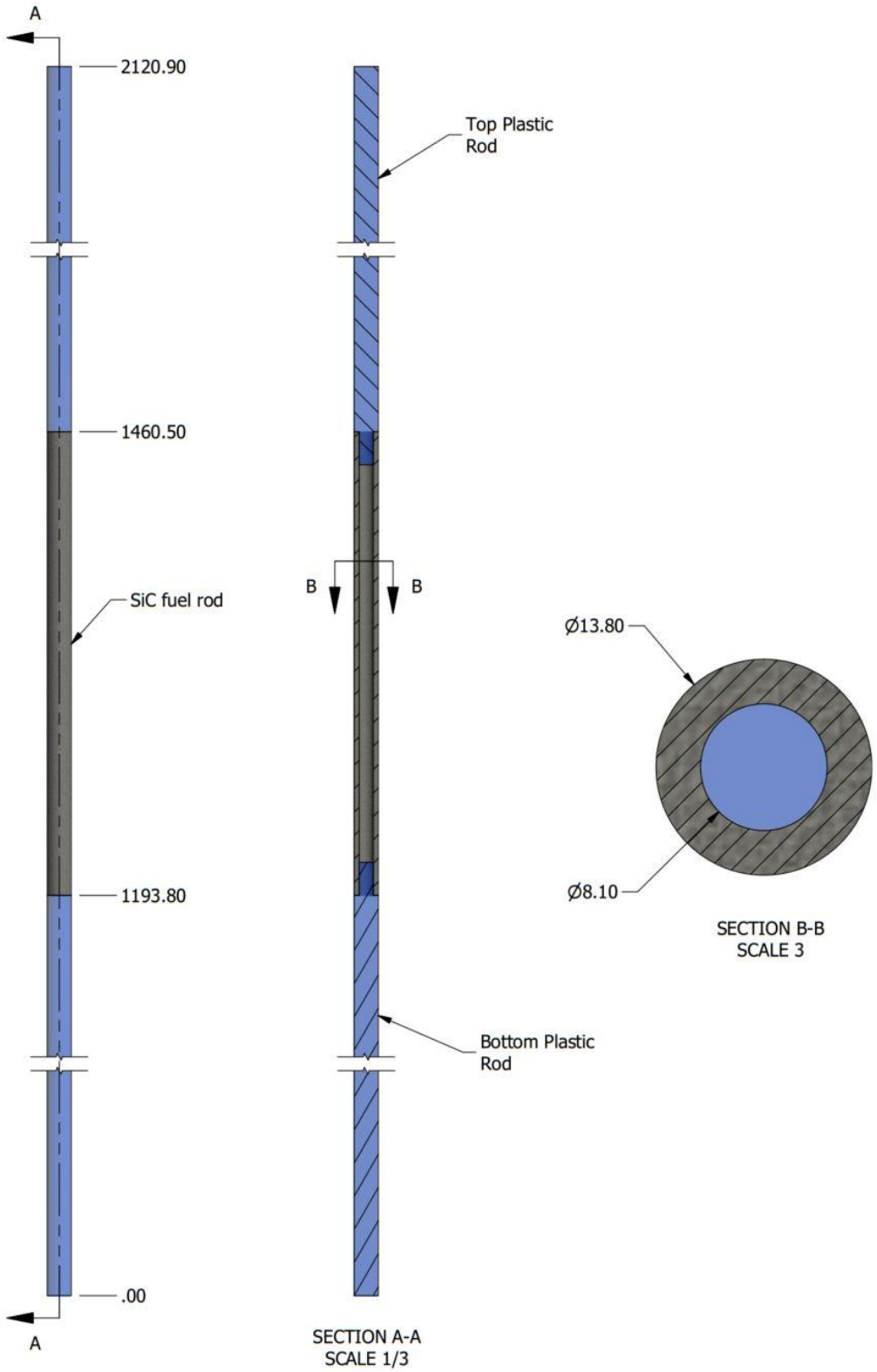

Figure 3.4 Single Simulated Fuel Rod (Dimensions in mm)

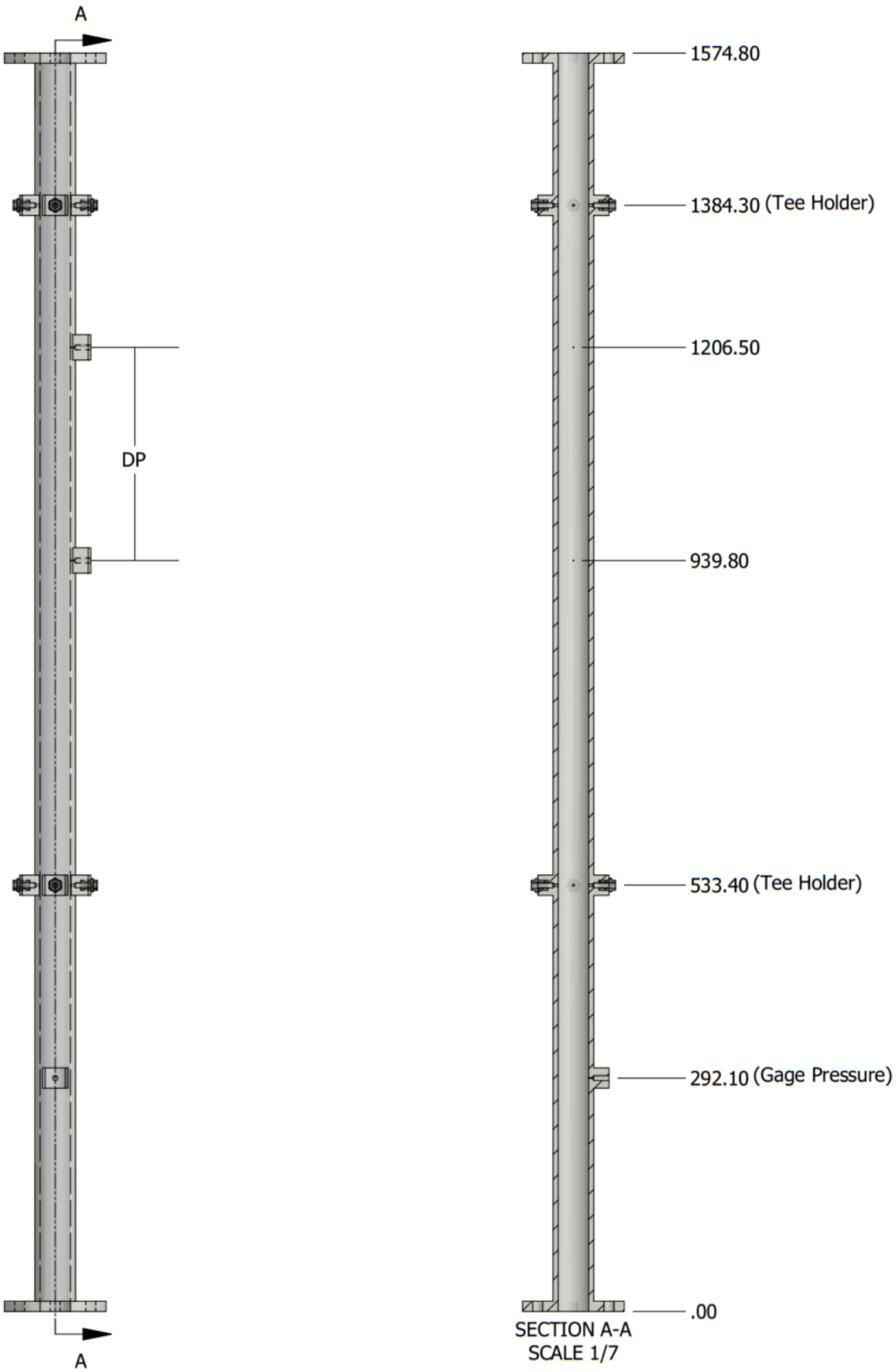

Figure 3.5 Flow Housing (Dimensions in mm)

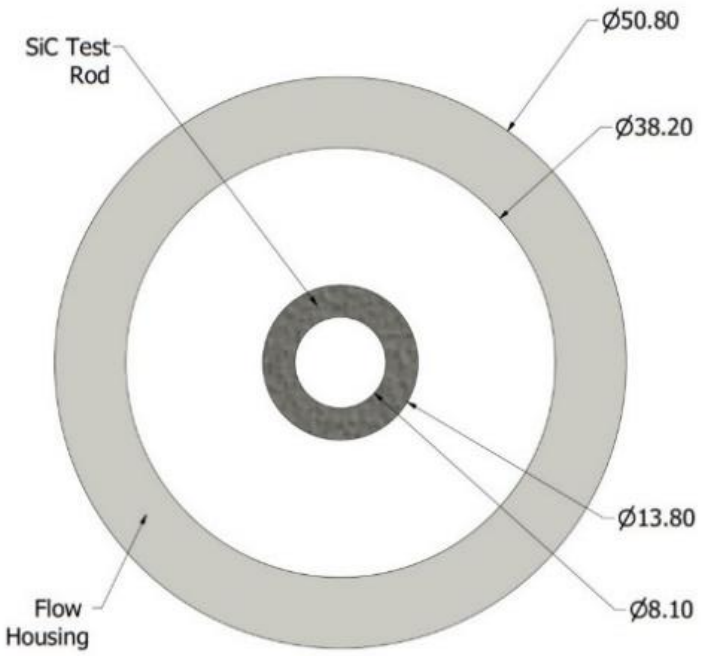

Figure 3.6 Cross Section of the Test Section

The shroud tube is fabricated of Acrylic (Plexiglass) tube with two flanges attached to either end which are in turn bolted to the loop tees. The shroud tube has an inner diameter of 38.2 mm and a wall thickness of 6.2 mm and is 1570 mm in length. Two pressure tap holes are drilled at selected locations along the axial length of the shroud tube to monitor pressure drop across the SiC fuel rod. Another pressure tap is drilled twenty-five (25) hydraulic diameters upstream from the lower end of the single simulated fuel rod section, to measure the operating gage pressure during tests. Quarter (0.25) inch stainless steel tubes connect the pressure tap holes to the pressure transmitters outside the flow housing

To ensure that the single simulated fuel rod is aligned with the centerline of the annulus of the shroud tube the flow housing has two (2) sets of rod supports each ten (10) hydraulic diameters upstream and downstream from the SiC fuel rod. Each set has four (4) sets of stainless steel rods each of 50 mm length and 3 mm diameter.

3.3 Silicon Carbide Fuel Rod

The SiC fuel rod used for the investigation was provided by Westinghouse. The relatively thin wall tubes fabricated for this work are constructed of 2 layers; an inner thin wall SiC monolith tube surrounded by SiC_f/SiC CMC. The inner thin wall monolith tube is used to obtain reasonable inner diameter dimensional tolerance for a nuclear fuel cladding tube and a hermetic seal [2]. The outer SiC_f/SiC CMC is used to provide strength and some amount of durability to a fully ceramic tube. Tubes were designed to have adequate mechanical properties for normal reactor operating conditions and a design basis accident, and to withstand impact during handling of a SiCf/SiC CMC tube filled with uranium dioxide (UO_2) fuel pellets. The roughness on the fuel rod was produced by braiding SiC fiber over the thin wall SiC monolith tubes, depositing a thin pyrolytic carbon (C) layer onto the braided fiber, and chemical vapor infiltration (CVI) of SiC into and on the braided fiber. Thus, the surface roughness design on the SiC fuel rod is irregular. The SiC fuel rod is shown in Figure 3.7. The roughness produced on the SiC tube is irregular. The roughness height was measured by the "Basic Bench Contour Projector" (shown in Figure 3.8) at USC. The height of the roughness was measured every 2.667 mm along the entire length (266.7 mm) of the SiC rod. A total of 100 readings were taken over the 266.7 mm length of the rod. Then the rod was rotated by an angle of 180 degrees and another set of 100 height readings were measured in a comparable manner. The contour plots obtained is shown in Figure 3.9. The average height of roughness of the rod is found to be 0.06155 mm and the root mean square of all the values is 0.07629 mm.

Figure 3.7 Roughness structure on the SiC Fuel Rod

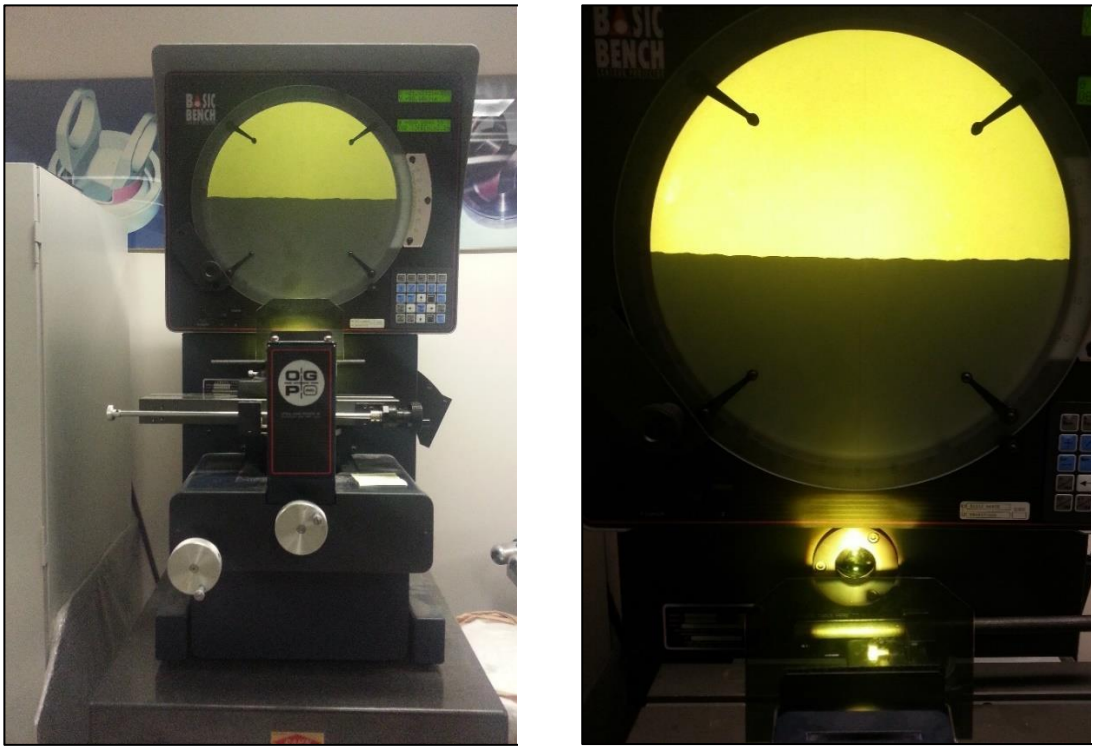

(a) (b)

Figure 3.8 (a) Basic Bench Contour Projector used for roughness measurement, (b) Display of the basic Bench Contour Projector

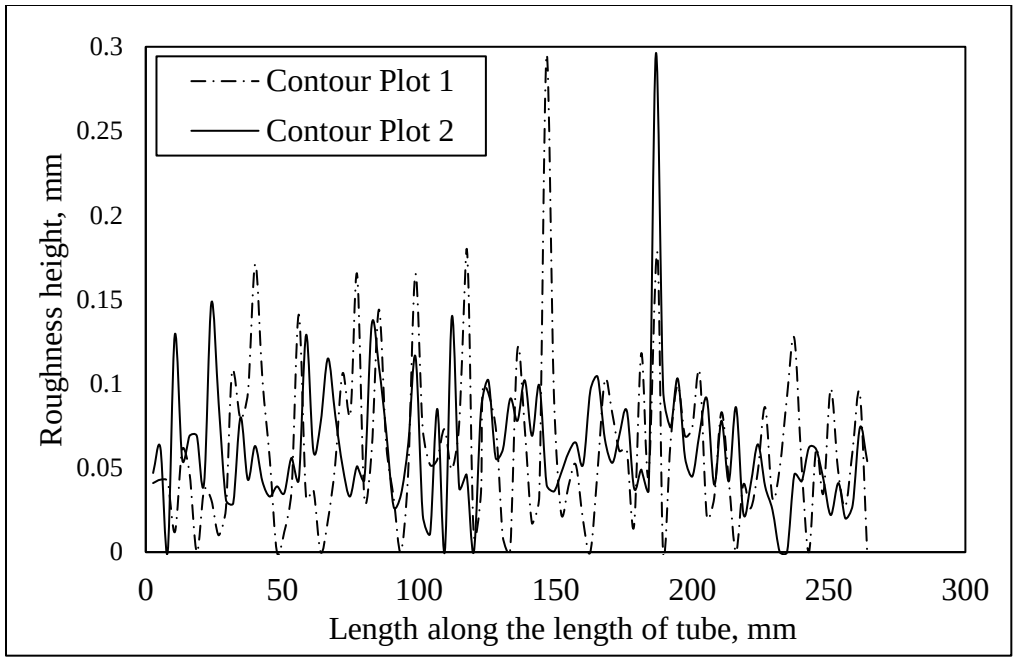

Figure 3.9 Contour plot for the SiC fuel rod surface

3.4 Test Fluid

The test fluid is deionized (DI) water for the following requirements:

Chlorides:	less than 0.2 ppm
Solids:	less than 0.5 ppm
Oxygen:	less than 0.1 ppm
pH:	6.5 to 7.5
Resistivity:	0.5 MΩ/cm (min.)

3.5 Pump

The pump is a 0.75 HP Grundfos model CRIE 10-1 unit, which is a vertical inline multi-stage booster pump with all wetted parts constructed from 304 series stainless steel, with a flow capacity of 15 m^3/h against a 10 m head. The pump is fitted with cool-top air-cooled shaft seal chamber and can handle water up to 180 ˚C.

3.6 Flow Meters

The loop includes three flow meters, two to measure the total flow rate through the test section at lower and higher flow ranges, and the third to measure the flow rate of the cooling water through the heat exchanger. The system flow meters are Cameron model NUFLO^{TM} 10 and 38 mm stainless steel turbine meters for lower (0.068-0.68 m^3/h) and higher (3.41-40.88 m^3/h) ranges, respectively, with magnetic pickups and silver soldered shaft and bearings to accommodate temperatures and pressures up to 230 ˚C and 1.3 MPa, respectively. The NUFLO^{TM} meter is connected to the data acquisition system. It includes an analyzer model MC-II Flow mounted directly on the flow meter for flow rate readings.

3.7 Heat Exchangers

After an hour or so of operation the water temperature in the loop rises due to viscous heating, even when no heat is applied to the simulated fuel rod. When the heated water exits the test section, it flows through the loop piping and then through the heat exchanger for cooling to the desired inlet temperature. The heat exchanger is a single-pass 76 mm diameter unit with the shell and the tube sides constructed from 316 stainless steel and heat transfer area of 1 m^2.

3.8 Compressor

A column of air, pressurized by a 0.026 m^3/0.9 MPa compressor, sets the system pressure. The pressurizer is constructed from 304 stainless steel piping partially filled with water above the loop.

3.9 Valves

The SHELT loop bypass and test section valves are 38 mm 316L stainless steel ball valves that control the water flow rate in the loop. One is located at the exit of the flow rate control bypass; one is located at the test section inlet temperature control bypass; and the other at the exit of the test section. A 19-mm precision valve made of brass controls the water flow rate at the exit of the heat exchanger.

3.10 Gage Pressure Transmitter

The gage pressure in the Loop is monitored at the bottom of the test section by a Rosemount 2051CG gage pressure transmitter (Figure 3.10). The 4-20 mA current output from the transmitter is calibrated between 0-2.07 MPa pressures and it can withstand temperatures of up to 150˚C. The transmitter has a LCD screen display and it is also connected to the data acquisition system.

3.11 Differential Pressure Transmitter

A Rosemount 2051CD pressure transmitter measures the axial flow resistance across the SiC fuel rod (Figure 3.10). The 4-20 mA current output from the pressure transmitter is calibrated between pressures of 0-4.2 KPa. Just like the gage pressure transmitter the differential pressure transmitter also has a LCD display and its outputs are also connected to the data acquisition system.

3.12 Thermocouples

Two OMEGA thermocouples (K-types) are inserted in the pipe through press fittings, the tips of the probe thermocouple are maintained in the middle of the pipe. First thermocouple gives the temperature reading of DI water going into the test section and the

second thermocouple gives the temperature of the fluid leaving the test-section. All the thermocouples are connected to a Data Acquisition system. LabVIEW 8.6 is used to collect temperature readings on the computer.

Figure 3.10 Rosemount Gage and Differential Transmitters

3.13 Processing System

The processing system used for experiments is a Desktop Computer with specifications as under:

Microsoft Windows XP professional version 2002. service pack 2002

Processor: 2.81 GHz

RAM: 3GB

A National Instruments (NI DAQ-9172) Data Acquisition System as shown in Figure 3.11 is used to acquire the signals from thermocouples and pressure transducers. NI-9172 DAQ card is used to convert voltage signals from thermocouples whereas NI-

9203 DAQ card is used to convert current signals from pressure transducers into readings that are collected on the Computer using LabVIEW 8.6 software. A screen shot of LabVIEW program is shown in Figure 3.12.

Figure 3.11 NI Data Acquisition System

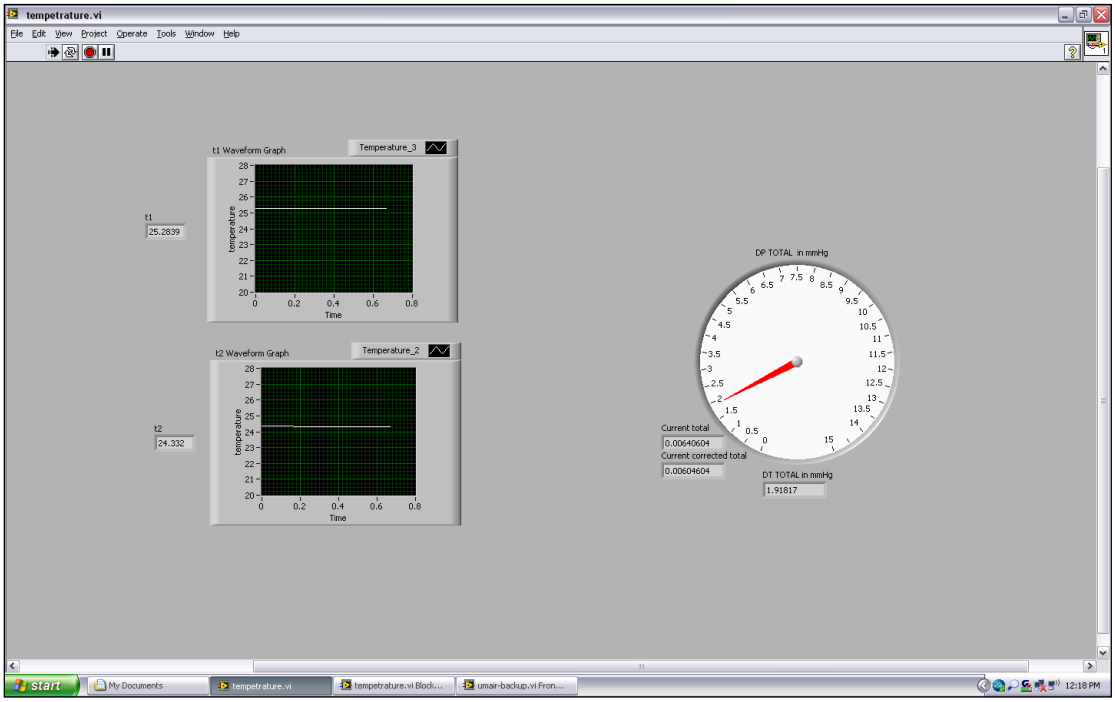

Figure 3.12 The LabVIEW Program Interface

CHAPTER 4

TEST PLAN AND DATA REDUCTION

4.1 Pressure Drop Cold Test

The pressure drop test is conducted to quantify the pressure drop over the length of the SiC rod. The test is conducted in steady state conditions. The nominal ranges of the parameters are:

Water Flow Rate: 0.1 - 14 m^3/h

System Pressure: 0.1 MPa

Water Temperature: 20±10 ˚C

A cold flow pressure drop test is performed at the beginning of the experimental program prior to the heat transfer tests. The readings will be taken at nine (9) different flow rates with ten (10) readings of differential pressure difference at each flow rate. These tests are performed at gage pressure of 0.1 MPa and at temperatures of 20 ± 10 °C. The following nine (9) flow rates are sequentially run in the cold test:

4.5	5.5	6.5	7.5	8.5	9.5	10.5	11.5	12.5	Flow-Rate (m^3/h)
4491	5489	6487	7485	8483	9481	10479	11477	12475	Mass Flux (kg/h)

4.2 Test Plan

The SHELT loop is filled with water and the pump is turned on and the flow rate is set to the lowest value. The loop is run until it reaches steady state and all the bubbles are evacuated from the system. Bleed valves present in the pressure transmitters and one at the top of the test section are opened intermittently to rid the bubbles from the loop. A bubble

free system is confirmed by looking closely at the test section through the transparent Plexiglas flow housing. Temperatures at the inlet and outlet of the test section are monitored by two K-type thermocouples, which are connected to the LabVIEW computer through the NI DAQ. The loop is considered to have reached steady state when the temperature readings of the inlet and outlet do not vary by more than $0.5^{\circ}C$ over a period of 20 minutes. Once steady state is achieved the reading of pressure drop are collected from the differential pressure transmitters. The same procedure is repeated by increasing the flow rate, and thus the readings for all nine flow rates are collected.

4.3 Control Test

Before testing the Silicon Carbide nuclear fuel rod a control test was carried out by using a fuel rod of similar dimensions to that of the SiC rod. This was done for dual purpose: first to compare the present results with those of previous experiments, thereby ensuring that the experimental setup is working correctly, and secondly to establish a reference for the results obtained with rough tubes. Similar strategies were employed by previous investigators [15]. This test is repeated 3 times to ensure repeatability of results.

4.4 Data Reduction

The flow rate (Q) was measured from the flow meters. The mean velocity was measured from the flow rate and the cross sectional area of the annulus of the test section

$$U_m = \frac{Q}{A_c} \tag{4.1}$$

Where, $A_c = \pi({r_o}^2 - {r_i}^2)$

The Reynolds Number was calculated as follows:

$$Re = \frac{U_m D_h}{\vartheta} \quad (4.2)$$

Where, $D_h = 2(r_o - r_i)$ and ϑ is the kinematic viscosity of the fluid.

The equation for friction factor is given as follows:

$$f = \frac{-2\left(\frac{\Delta p}{\Delta x}\right) D_h}{\rho {U_m}^2} \quad (4.3)$$

Where, $\frac{\Delta p}{\Delta x}$ is the pressure drop per unit length.

The friction factor obtained from the correlation [16] in equation 4.4 is compared with the experimental friction factor obtained for the smooth rod.

$$f = 0.184 Re^{-1/5} \quad (4.4)$$

Dimensions of the simulated Smooth and Rough Rods

Type of Rod	Diameter in m	Length in m
Smooth Rod	0.013758	0.2667
Rough SiC Rod	0.0135636	0.2667

For calculation purposes the following values were used:

ρ = 995.03 kg/m^3

ϑ = 0.801*10^{-6} m^{2}s^{-1}

4.5 Test Parameter Tolerance

Actual test conditions must meet the requirements provided in Section 4.1 within the following limits:

Water Flow Rate:	±0.07 m^3/h
System Pressure:	±1.55 KPa
Water Temperature:	±0.24 ˚C

4.6 Uncertainty Analysis

The experimental uncertainty was calculated using the Kline McClintock formula. This is given as:

$$U_f = \sqrt{\left(\frac{\partial f}{\partial \Delta p}\right)^2 {U_{\Delta p}}^2 + \left(\frac{\partial f}{\partial Q}\right)^2 {U_Q}^2} \quad 4.5$$

where $U_{\Delta p}$ is given as

$$U_{\Delta p} = \sqrt{\left(U_{accuracy}\right)^2 + (U_{random})^2} \quad 4.6$$

where, $U_{accuracy}$ is the uncertainty due to bias error of the instrumentation and U_{random} is the uncertainty due to the randomness of the obtained readings. The uncertainty for the investigation was found to be ±1.67%.

CHAPTER 5

CFD ANALYSIS

In this chapter, details will be provided on the development of a the CFD model. A 2D CFD model of the flow was created in ANSYS Fluent. The Fluent solver is based on the Finite Volume Method. The purpose of the CFD model is to: 1) Compare and validate the experimental results of friction factor for the SiC roughness design, 2) To numerically ascertain the heat transfer enhancement, 3) Get some insights into the flow mechanism that is involved which increases the heat transfer and pressure drop.

5.1 Flow Domain

The flow domain created for the CFD analysis is shown in Figure 5.1. A 3D CAD model (Figure 5.2) of the SiC Fuel rod was created in SolidWorks. This model was imported into the ANSYS workbench DesignModeler. The model was then modified to achieve the 2D flow domain as shown in Figure 5.2. The geometric design parameters for the rod are given in Table 5.1. It is to be noted that the geometric model of the roughness design created had some inherent errors. The actual SiC fuel rod was produced by vapor deposition and braiding, thus it had irregular bumps and very fine thread like features on its surface. These were difficult to measure thus they were ignored in the CAD design. So, the CAD model created for the roughness design was less rough than the actual SiC fuel rod. Thus, we expect the CFD results to give a lower approximation of the friction factor when compared to the experimental results.

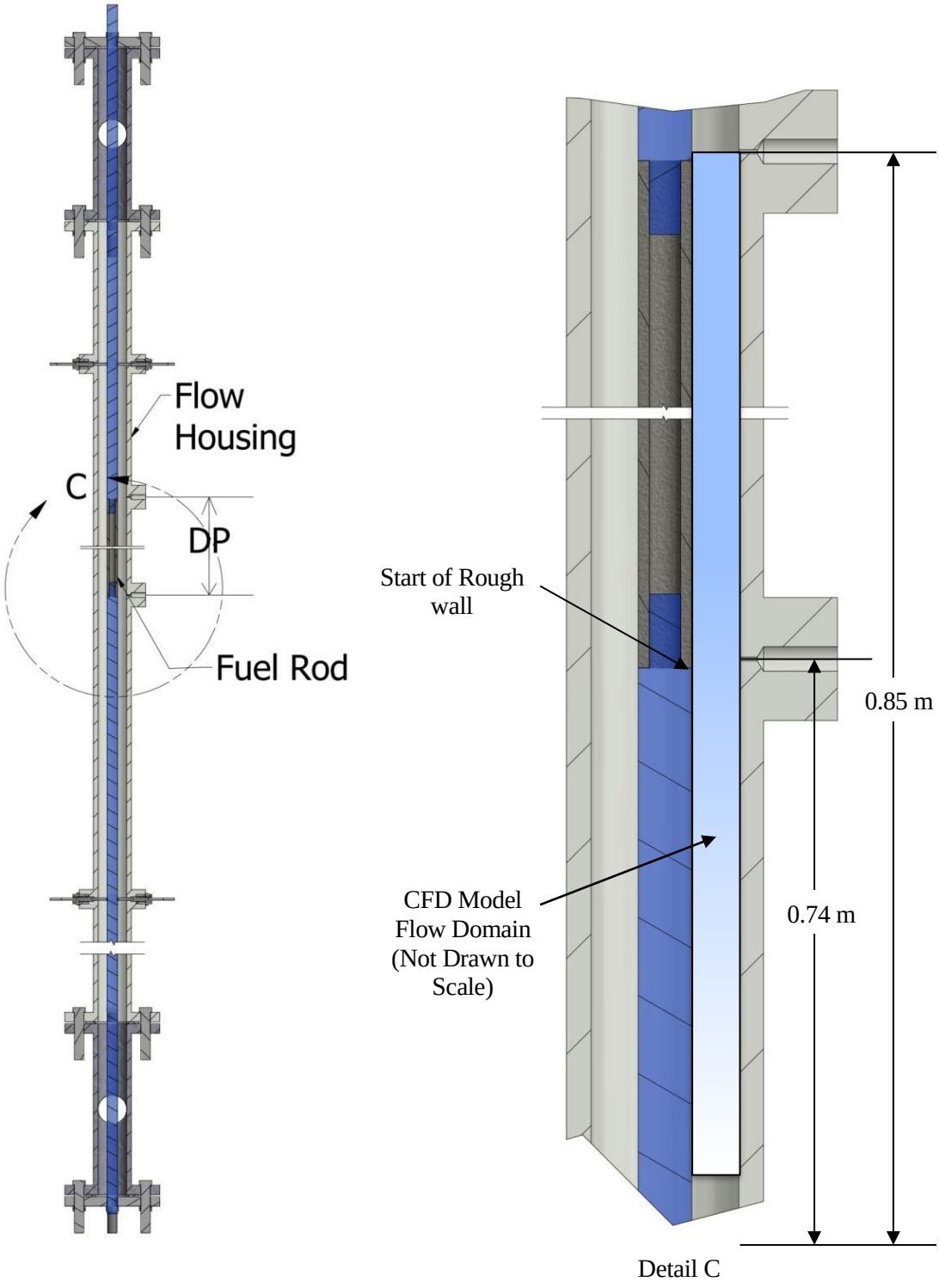

Figure 5.1 Flow Domain used for CFD Analysis

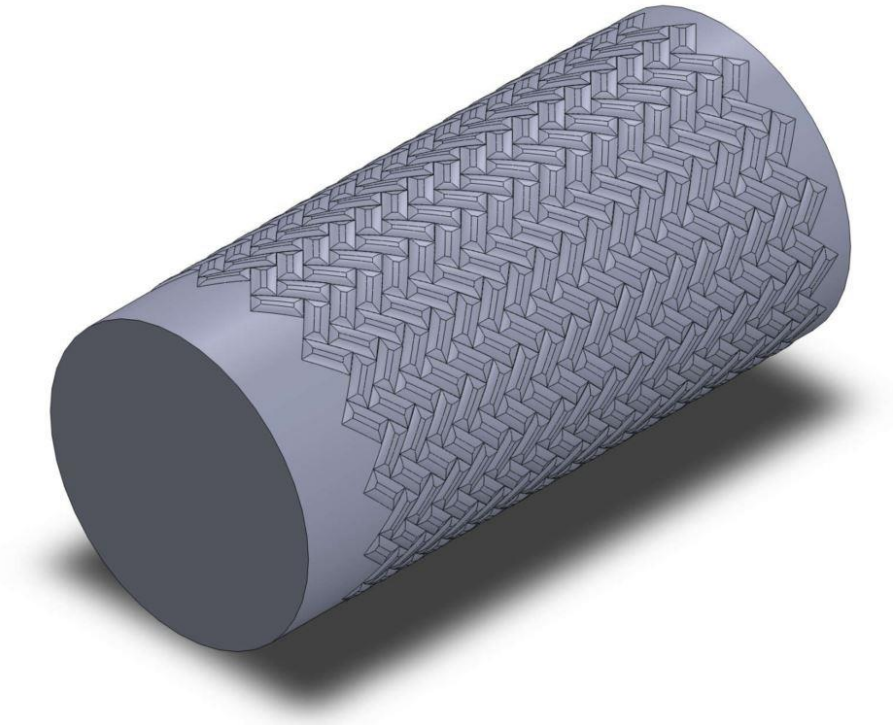

Figure 5.2 3D CAD model of the SiC Fuel Rod

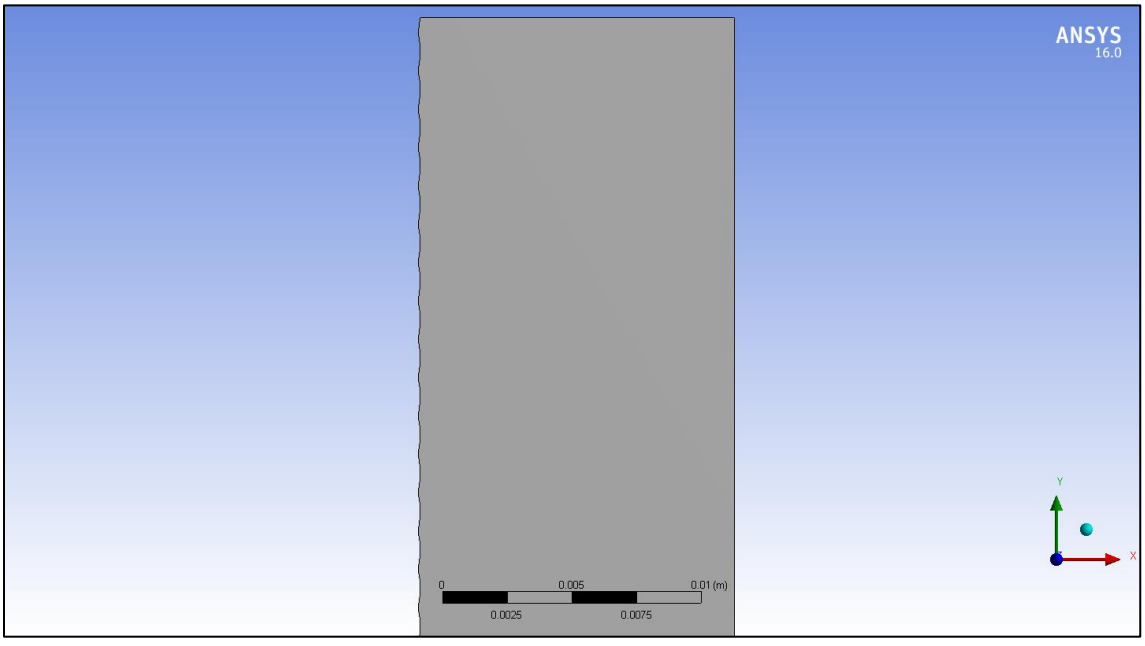

Figure 5.3 2D Flow Domain produced in ANSYS DesignModeler

Table 5.1 Geometric Parameters

Roughness height	0.07629
Hydraulic diameter	12.32
total tube length	850
entrance smooth length	750
rough length	100

5.2 Meshing

5.2.1 General Meshing Considerations

When creating a mesh there are some requirements that need to be considered as the results will be affected by the quality of the grid. Both stability and the accuracy is affected by poor quality mesh. Naturally a denser mesh is better, however mesh numbers must be kept at an optimum level to reduce computational times. Thus, denser meshing should only be used in regions of interest, especially where the change in field variables is rapid. Also, the change from small to large variables should be smooth so that there are no abrupt changes in the size of the grid cells. Areas of low interest where changes in field variables is relatively low can have larger elements thus keeping the total number of elements to a minimum.

5.2.2 Turbulent Flow Considerations

The flow to be modelled has a Reynolds number in the range of 10^4 to 10^5. Thus, it is completely in the turbulent flow range. Therefore, it is important to take some additional consideration while meshing.

In turbulent flows the near wall meshing is very important. To understand why it is so, we must consider the velocity profile of a turbulent flow. Figure 5.4 shows a comparison of fully developed turbulent flow with laminar flow in a channel. It is clearly visible that the velocity changes close to the wall in case of turbulent flow is more rapid.

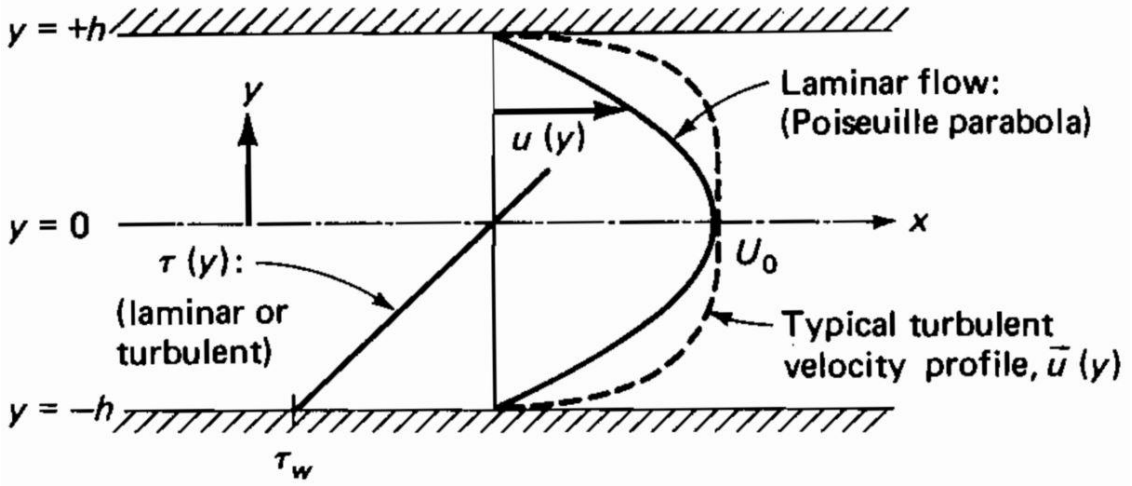

Figure 5.4 Comparison of fully developed laminar and turbulent flow in channel [17]

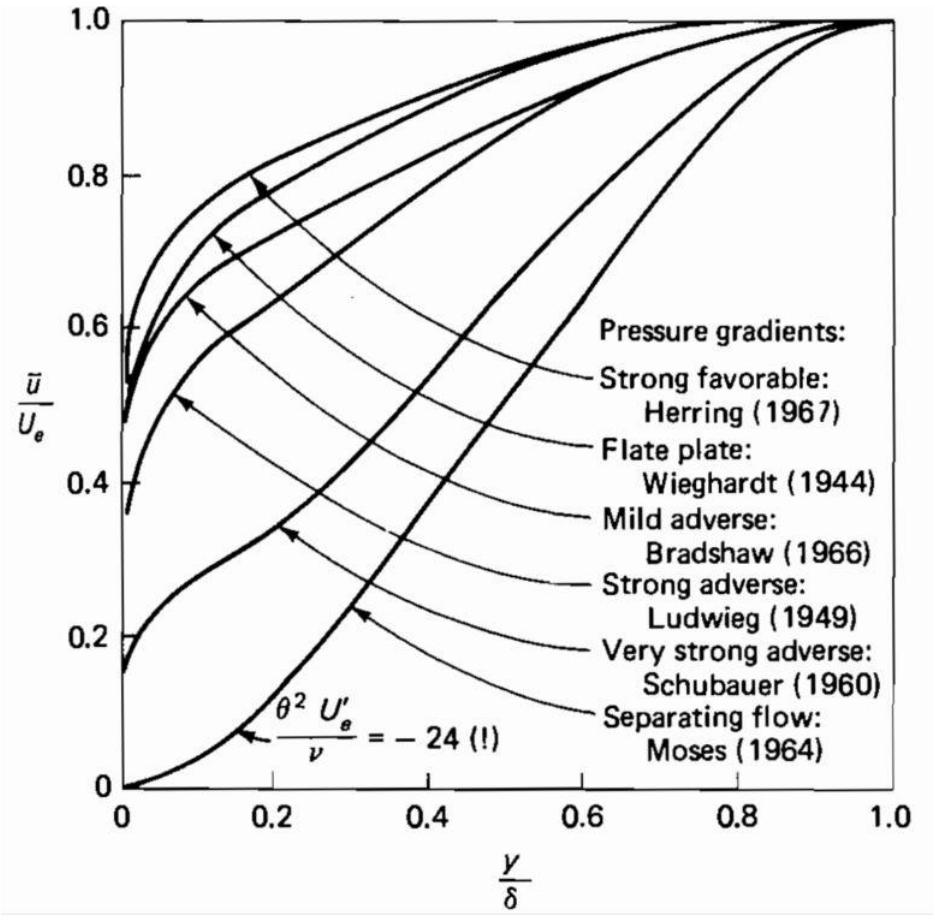

Figure 5.5 Experimental Turbulent boundary layer profiles for various pressure gradients [17]

Figure 5.5 shows experimental Turbulent boundary layer profiles for various pressure gradients. If we consider the graph for the strong favorable gradient it appears as if there is velocity slip in the wall. But there is no velocity slip. The velocity profile actually changes very rapidly to zero in a thickness that is very small ($0 \leq y/\delta < 0.002$). A better understanding of the boundary layer can be obtained by referring to Figure 5.6.

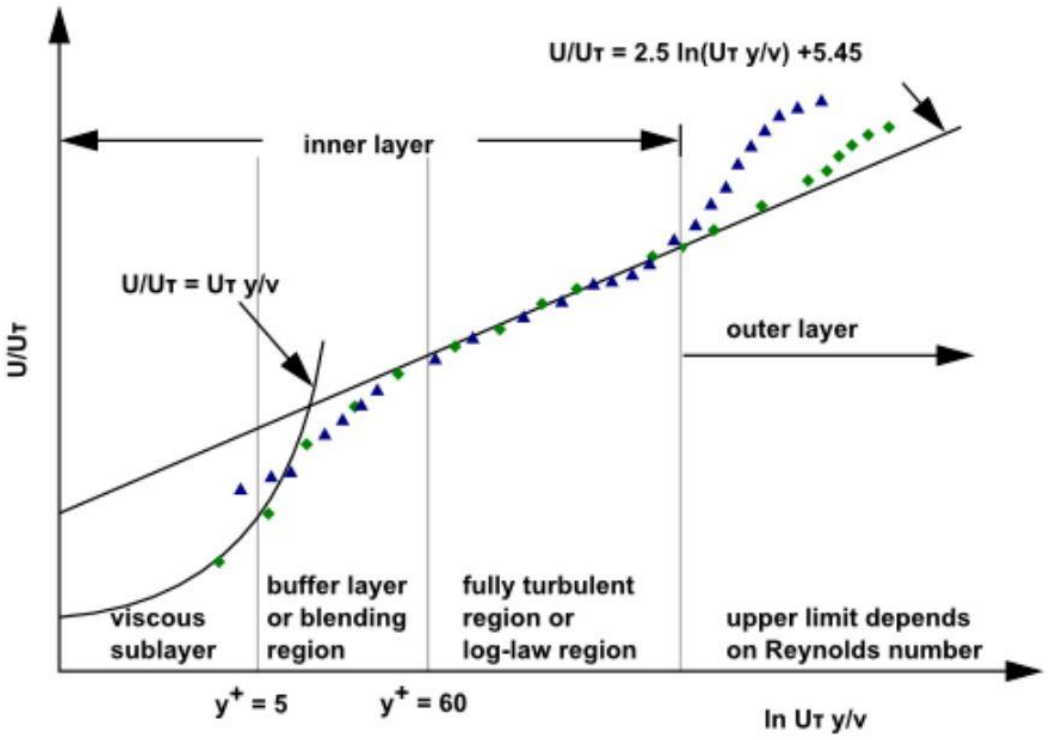

Figure 5.6 Subdivision of Near Wall Region[18]

Here the near wall region has been divided into subdivisions by introducing two new parameters (non-dimensional distance from the wall, y^+; the wall friction velocity, u_τ). The viscous sublayer near the wall which extends from y^+ values 0 to 5 is a region where viscous shear dominates. In the outer layer the Turbulent shear has the dominating effect.

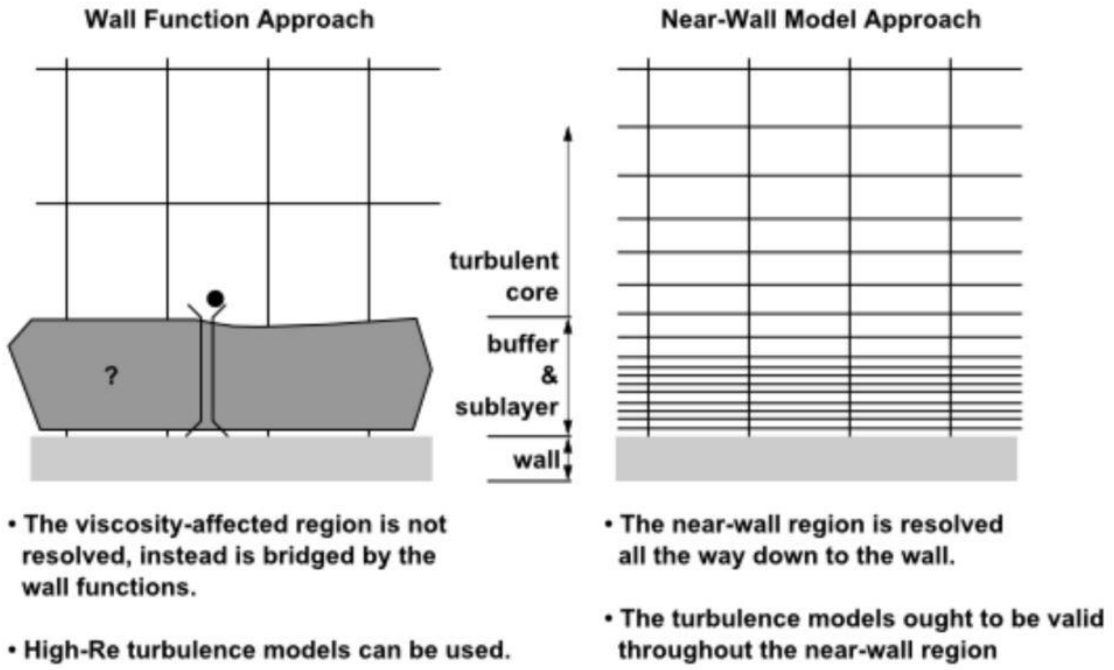

Figure 5.7 Near wall meshing approaches[18]

The meshing in the viscous sublayer is vital for getting accurate results in case of turbulent flows. There are two approaches for the near wall meshing (Figure 5.7):

1. Wall Function Approach: This does not solve the governing equations in the near wall region but uses functions. Thus, the near wall meshing need not be very fine.
2. Near-Wall Model Approach: In this approach, the near wall region is resolved by solving the governing equations. Thus, the mesh in that region needs to be very fine, and $y^+ \sim 1$ needs to be achieved. This was the approach that was taken for this CFD analysis.

5.2.3 Mesh Calculations

Calculations are needed to be performed to find the position of the first node (Δy) from the wall. To do this, first the friction factor value is needed to be assumed. For the smooth rod this was assumed by equation 4.4:

$$f = 0.184Re^{-1/5} \quad (4.4)$$

For the rough rod the equation proposed by Haaland [19] for sand grain roughness was used to assume the friction factor:

$$f^{-1/2} = -1.8log\left(\frac{6.9}{Re} + \left(\frac{k_s/D_h}{3.7}\right)^{1.11}\right) \quad (5.1)$$

Where D_h is the Hydraulic Diameter and k_s is the sand grain roughness height (taken as 0.07629 mm). For both the smooth and the rough SiC rod the following calculations are performed to obtain the position of the first node of the mesh from the wall to satisfy the y+ requirements.

$$C_f = 0.25f \quad (5.2)$$

$$\tau_w = 0.5C_f\rho{U_m}^2 \quad (5.3)$$

$$U_\tau = (\frac{\tau_w}{\rho})^{0.5} \quad (5.4)$$

$$\Delta y = \frac{y^+\vartheta}{U_\tau} \quad (5.5)$$

Where for water at 30˚C,

ρ = 995.03 kg/m^3, ϑ = 8.01e-7 m^{2}s^{-1}

Both triangular and quadrilateral elements were used in order to mesh the flow domain. The near wall region of the wall was meshed by using the inflation option in the ANSYS Workbench Meshing. The area in the free stream of the domain was meshed by using triangular elements. At first a coarse mesh was used. This mesh was improved and made finer until mesh independence was achieved. Mesh independence study was made by comparing 4 mesh models with 1530233, 1932818, 3011863 and 3908981 elements.

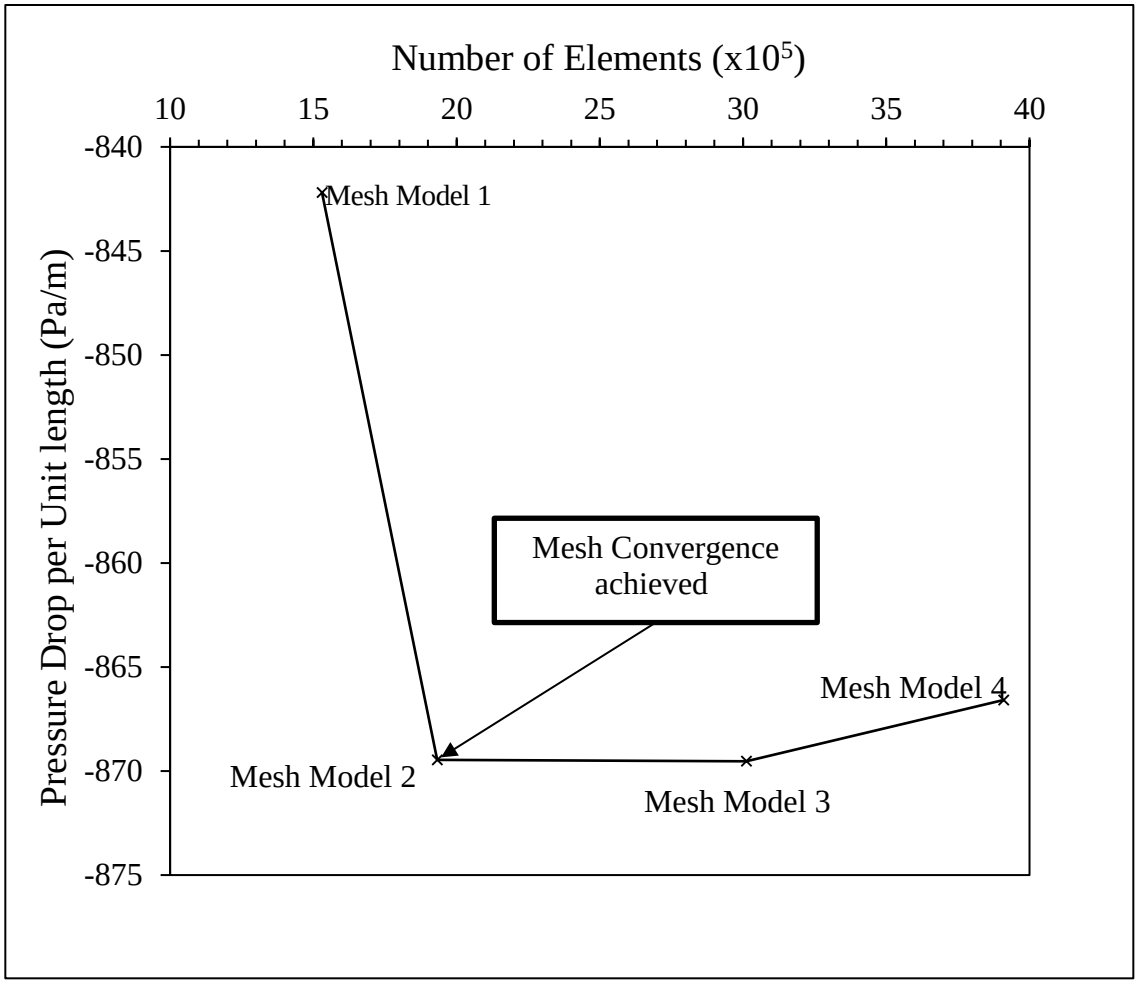

Figure 5.8 Grid Independence study

Table 5.2 Meshing Parameters

near wall	
first layer thickness	0.0023
number of inflation layers	32
growth rate	1.1
y+ covered	0.6 ~ 120
freestream region	
maximum face size	0.1
minimum face size	0.0006

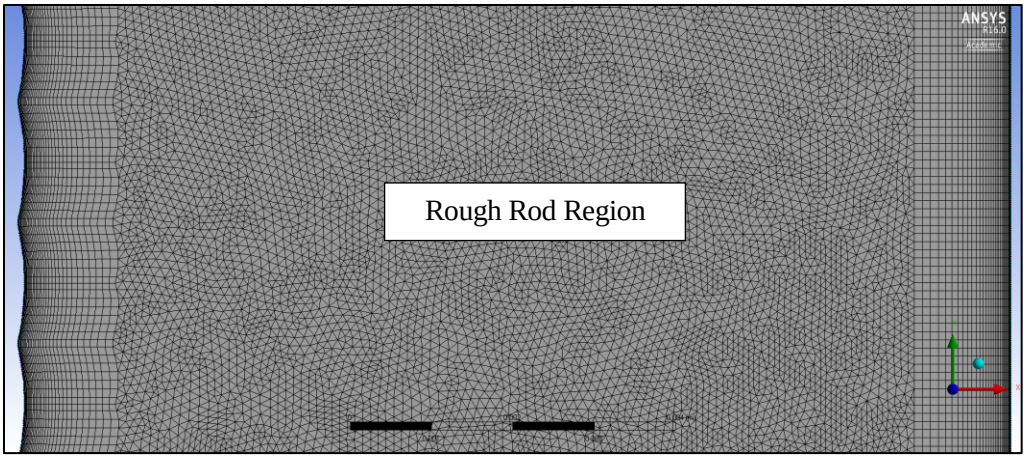

Figure 5.9 Meshing in rough region

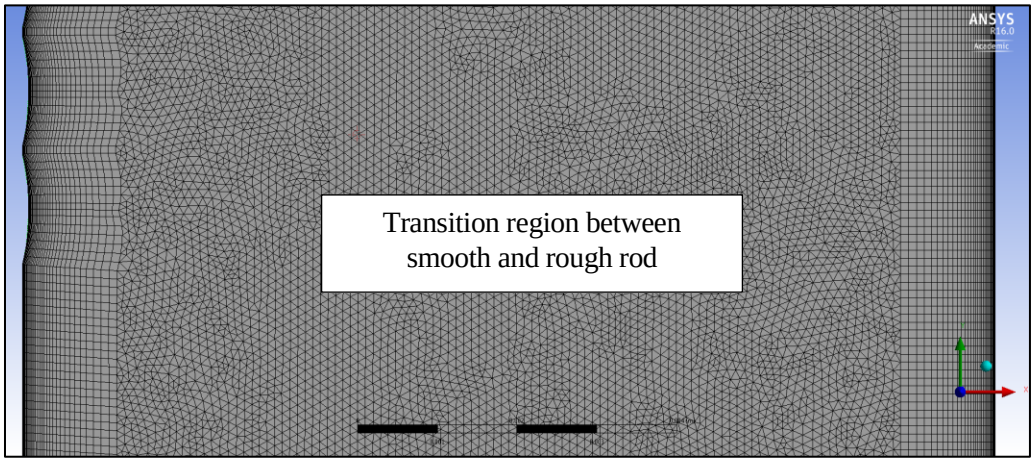

Figure 5.10 Mesh in the transition region between smooth and rough rod

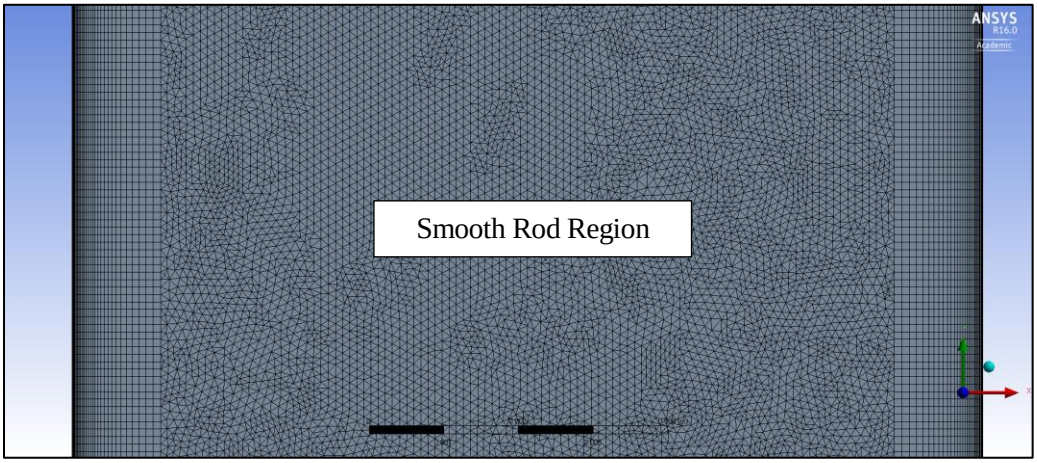

Figure 5.11 Meshing in smooth Region

As seen in Figure 5.8 the Pressure drop per unit length between the Model 1 and Model 2 increased by 3%. For Mesh Model No. 2 and 3 the Pressure Drop per unit length is almost the same. Therefore, the mesh independence is achieved at Mesh Model No. 2. This is further confirmed since after mesh model no. 4 with 3908981 elements we see that the Pressure Drop per unit length decreases. Figure 5.9 to Figure 5.11 shows the mesh model used for one of the flow rates.

5.3 Numerical Methods

5.3.1 Governing Equations

This section will introduce the governing equations used to solve the fluid flow and heat transfer inside the computational domain. The flow field solutions are obtained by solving the time averaged continuity and momentum equations in 2D. The time averaged energy equation is solved to obtain the heat transfer analysis.

The steady state continuity equation which expresses the conservation of mass for an incompressible fluid is defined as:

$$\boldsymbol{\nabla} \cdot \bar{V} = 0 \tag{5.6}$$

The Reynolds Averaged Navier Stokes (RANS) equation is as:

$$\rho \frac{D\bar{V}}{Dt} = \rho g - \nabla \bar{p} + \nabla \cdot \tau_{ij} \tag{5.7}$$

Where,

$$\tau_{ij} = \mu \left(\frac{\partial u_i}{\partial x_j} + \frac{\partial u_j}{\partial x_i} \right) - \rho \overline{u'_i u'_j}$$

The Energy Equation is expressed as:

$$\rho C_P \frac{D\bar{T}}{Dt} = -\frac{\partial}{\partial x_j}(q_i) + \overline{\emptyset} \tag{5.8}$$

Where,

$$\overline{\emptyset} = \frac{\mu}{2}\overline{\left(\frac{\partial \overline{u_i}}{\partial x_j} + \frac{\partial u_i'}{\partial x_j} + \frac{\partial \overline{u_j}}{\partial x_i} + \frac{\partial u_i'}{\partial x_j}\right)^2}$$

$$q_i = -k\frac{\partial \overline{T}}{\partial x_i} + \rho C_P \overline{u_i' T'}$$

It is to be noted that the time averaging of the Navier Stokes equations introduced new unknowns into the flow equations through the τ_{ij} term. Thus, new equations needs to be solved to find the new unknowns.

The procedure of solving the new unknowns is known as turbulence modeling. There are a number of turbulence models, and one of them is called the *k*-ω shear stress transport (SST) model [20], [21], which is used in this analysis. This model uses the advantages of both the *k*-ε and the *k*-ω models. The *k*-ω model is more accurate near the wall layers, and has been successful with flows with moderate adverse pressure gradients. However, the ω equation shows sensitivity to the values of ω in the freestream outside the boundary layer [22]. The *k*-ε model is more accurate in the freestream region away from the wall. The SST model divides the flow domain into two regions, and it uses blending functions to switch between *k*-ε and *k*-ω models. The *k*-ω SST model is also a better choice when compared with the wall functions since it solves the flow equations near the walls, and thus reveals flow characteristics in the near wall region. One of the drawbacks of using SST model is that it requires a very fine mesh in the laminar sublayer region extending up to the buffer layer. This requirement significantly increases the computation effort. Hence, this analysis uses a dense and structured mesh for near wall regions.

5.3.2 Solution Procedures

The Fluent solver is used to solve the governing equations by using a steady state Pressure-based solver. The pressure based solver uses an algorithm where the mass conservation of the velocity field is achieved by solving a pressure equation. The pressure equation is derived from the continuity and momentum equations so that the velocity field corrected by the pressure satisfies continuity. The governing equations are nonlinear and coupled to one another. Thus, a solution is obtained by iteration of the complete set of governing equations until convergence is obtained.

A step by step solution strategy was employed for the computational analysis. The flow equations (continuity and RANS) do not have any temperature terms, thus they can be solved to convergence at first. Then the heat equation is turned on and all the equations are solved to convergence.

The Boundary Conditions (BC) were set as shown in Figure 5.12. The inlet BC was set as velocity inlet, and a temperature of 303 K was set. A constant heat flux of 232509 W/m^2 was set at the inner wall. A turbulent intensity of 5% and turbulent length scale of D_h was set at the inlet to calculate the initial guess values of k and ω. The solution methods were set up as shown in Figure 5.13.

To simulate the experimental results correctly a fully developed flow must be established before flow hits the rough section. To ensure this numerically a line was plotted vertically along the center of the flow domain. The velocity was plotted along this line as shown in Figure 5.14. The velocity initially increases as y increases and then it remains constant until the flow hits the rough section. Fully developed conditions are achieved at the point shown in the Figure 5.14.

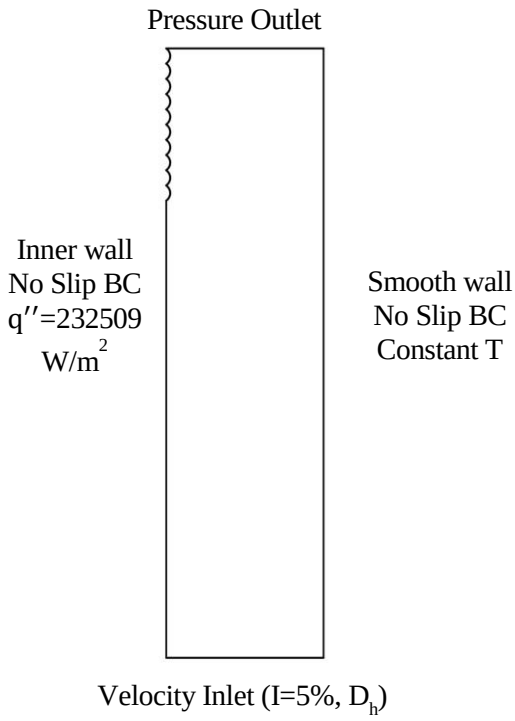

Figure 5.12 Boundary Conditions

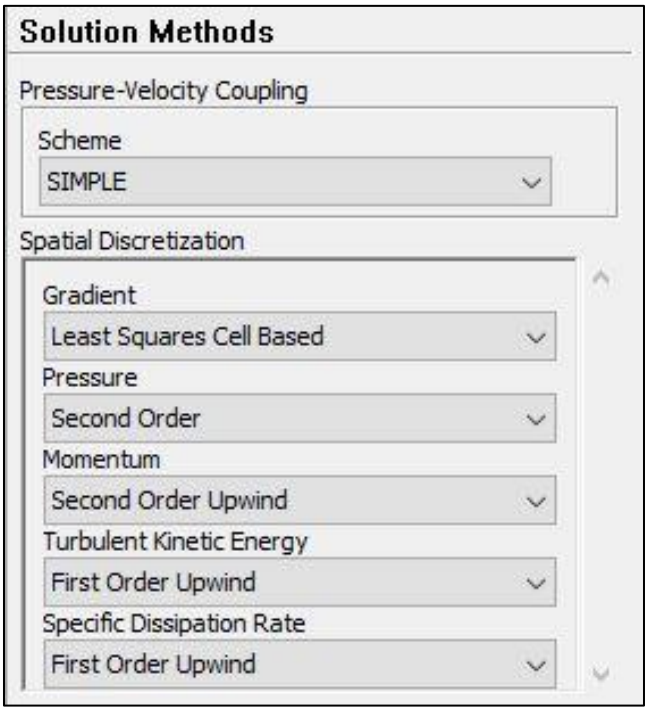

Figure 5.13 Finite Difference Schemes used for discretization of the various terms in the governing equations

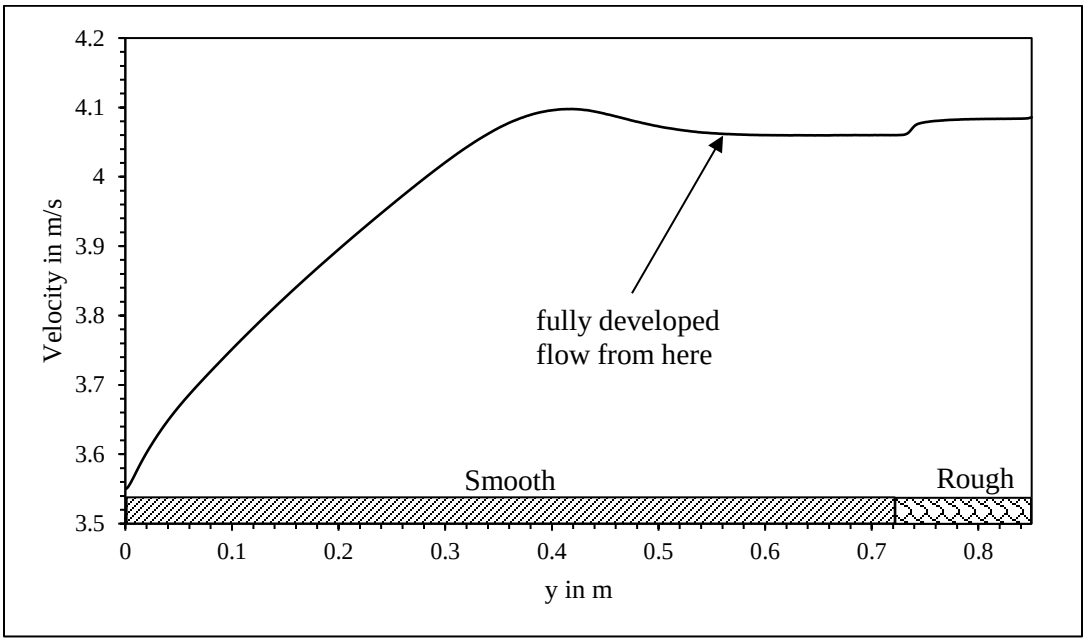

Figure 5.14 Velocity vs. y (elevation) drawn along center of flow domain

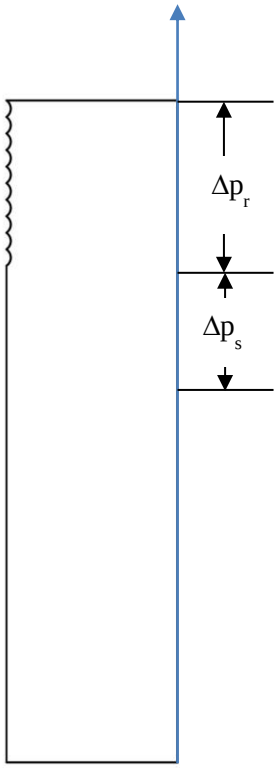

Figure 5.15 Locations where pressure drops are measured

5.4 Data Reduction

5.4.1 Friction Factor Calculations

The friction factor results from CFD for the smooth section was compared with the correlation in equation 4.4.

The CFD results for the friction factor in the smooth and rough section is calculated using the following formula:

$$f = \frac{-2\left(\frac{\Delta p}{\Delta x}\right) D_h}{\rho {U_m}^2} \tag{5.9}$$

5.4.2 Heat Transfer enhancement calculations

For the computation of the heat transfer enhancement for the smooth section the following calculations were performed:

$$T_{b_1} = \frac{1}{D_h}\int_0^{D_h} T(x)\, dx \tag{5.10}$$

$$h = \frac{q''}{(T_w - T_{b_1})} \tag{5.11}$$

$$Nu = \frac{hD_h}{k_f} \tag{5.12}$$

Where T_{b_1} and T_w were measured at the locations shown in Figure 5.16.

The heat transfer enhancement for the smooth section were compared with the Gnelinksi Correlation [23]:

$$Nu = \left[\frac{\left(\left(\frac{f}{8}\right)(Re - 1000)Pr\right)}{1 + 12.7\left(\frac{f}{8}\right)^{\frac{1}{2}} Pr^{\frac{2}{3}} - 1}\right] \tag{5.13}$$

The following calculations were performed in order to calculate the Nusselt Number from the rough section of the rod:

$$T_{b_2} = \frac{1}{D_h}\int_0^{D_h} T(x)\,dx \tag{5.14}$$

$$T_{b_{avg}} = \frac{T_{b_1} + T_{b_2}}{2} \tag{5.15}$$

$$h = \frac{q''}{(T_{w_r} - T_{b_{avg}})} \tag{5.16}$$

$$Nu = \frac{hD_h}{k_f} \tag{5.17}$$

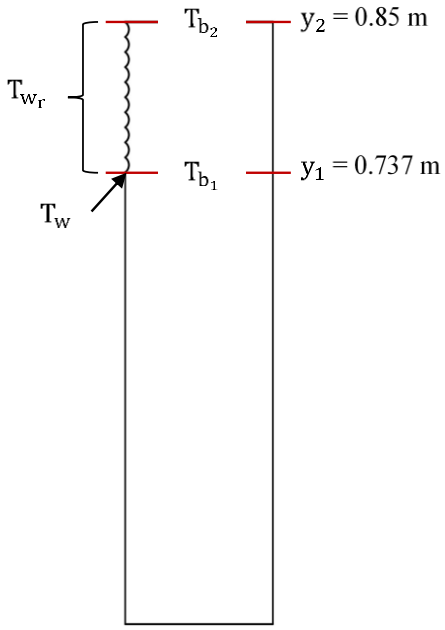

Figure 5.16 Heat Transfer Calculations

CHAPTER 6

RESULTS

6.1 Experimental Results

6.1.1 Pressure Drop Results for Smooth Rod

The loop was first run with the smooth rod. The data for pressure drop were collected over the nine different flow rates. In total four sets of results were collected to ensure repeatability of the results as outlined in section 4.1. All data were collected at temperatures and pressures of 30 ˚C and 0.05 MPa, respectively.

These data obtained from the experiment were then compared with the Correlation in equation 4.4. In Figure 6.1 friction factor is plotted as a function of the Reynolds number, and the experimental data for smooth rod from the three test runs are compared with that from correlation. The maximum recorded deviation between the experimental results and the correlation is ±2.36%. Taking into consideration the calculated uncertainty for the obtained value of friction factor, we can safely conclude that the experimental values agree well with the correlation. Looking at the graph we can also conclude that it passes the repeatability criteria.

6.1.2 Pressure Drop Results for Rough Rod

The pressure drop results for the SiC rough rod are shown in Figure 6.2. The obtained points for friction factor pass the repeatability tests and shows that friction factor drops as Reynolds number increases, as was the case with the smooth rod. However, the

rate of fall of friction factor with increase in Reynolds Number is lower when compared with that of the smooth rod. At the lowest investigated Reynolds No. of 40,000 a friction factor increase of 7.6 % is observed and at the highest Reynolds No. of 110,000 the friction factor increase was 15%, when compared with the smooth rod.

6.2 Numerical Results

6.2.1 Validation of the numerical model

Validation of the CFD model developed in ANSYS Fluent was done by comparing the CFD results for friction factor of the smooth section with that obtained from correlation in equation 4.4. Figure 6.3 plots the friction factor for the smooth section obtained from the CFD model compared to that obtained from the Correlation. The CFD results for the friction factor for smooth section shows a maximum deviation of ±4% from the correlation.

Figure 6.4 shows the results of friction factor for the SiC roughness design obtained from the experiments and from the CFD model. It is clearly noticed that the CFD analysis gives a lower estimation of the friction factor. This was expected for reasons explained in section 5.1. The maximum deviation from the experimental results is 8%, which occurs at the highest Reynolds Number.

Figure 6.5 shows the results for the Nusselt Number from CFD analysis and from the Gnielinski Correlation. It is observed that the Nusselt number increases when the Re No. increases which is due to the viscous sublayer becoming thinner. The viscous sublayer can act as an obstruction to the heat transfer from the hot fuel rod walls. Results for Nusslelt Number are also found to lie very close to those suggested by Gnielinksi Correlation. A maximum deviation of 9.9% is recorded.

From these results we can safely conclude that the CFD model is validated and thus can be used to compute the expected heat transfer enhancement that can be achieved by the SiC roughness design.

6.2.2 Numerical Results of Heat Transfer enhancement for SiC roughness design

Figure 6.6 and Figure 6.7, shows the flow characteristics around the roughness structures. Figure 6.6 shows the streamlines and the pressure contour plots for the case with Reynolds number 102436. From the figure recirculation zones/boundary layer separation is clearly identified. Adverse pressure gradients exist at points where recirculation is identified. Adverse pressure gradient is a necessary condition for flow separation. Flow separation occurs when the adverse pressure gradient along with the shear from the wall creates enough opposing resistance to the flow, to overcome the forward momentum of the fluid particles and cause them to flow in reverse direction. It is interesting to note that at a small distance away from the roughness structures towards the freestream, the streamlines become almost parallel and the roughness has no effect on the flow. The total resistance on the roughened surface is made up of the pressure forces and the skin-friction forces. The skin friction depends on the wall shear stress distribution. The pressure forces depend on the size of the wake formed beyond the separation point. The wake is a low-pressure region and a bigger wake formation results in a higher pressure drag.

Figure 6.7 shows the isotherms and the streamlines near a typical roughness element. It is found that the temperature of the water near the recirculation region is the highest and attains maximum near the point where separation begins. The temperature of water near the reattachment point is lower. Thus, near reattachment points the heat transfer from the wall to the water is the highest. Figure 6.8 shows the wall temperature variations

along the rough fuel rod wall. It is seen that in the smooth section the wall temperature increases slowly but in the rough region the wall temperature is fluctuating rapidly. Thus in order to find the actual overall heat transfer enhancement the average is to be found for the entire roughened region of the SiC rod.

The results for Nusselt number are obtained from the CFD model for six values of Reynolds number in the range $5x10^4$ to $1.1x10^5$. For each Reynolds Number investigated the Nusselt Number is measured using the calculations as outlined in section 5.4.2.

Figure 6.9 shows the comparisons of Nusselt Number for the smooth and the rough rods. It is observed that the Nusselt number for the rough rod is always greater than that obtained for the smooth rod. A maximum heat transfer enhancement of 18.4% can be achieved with the rough rod at the highest Reynolds Number investigated. The surface roughness structures in the fuel rod promotes turbulence which enhances heat transfer by breaking the thermal boundary layer and stimulating turbulent mixing. However, we can expect that in actual practical application the roughness design will provide a heat transfer enhancement greater than 18.4% for reasons explained in section 5.1.

Figure 6.10 to Figure 6.13 shows the contour plots of Pressures and Temperatures in the rough and smooth sections

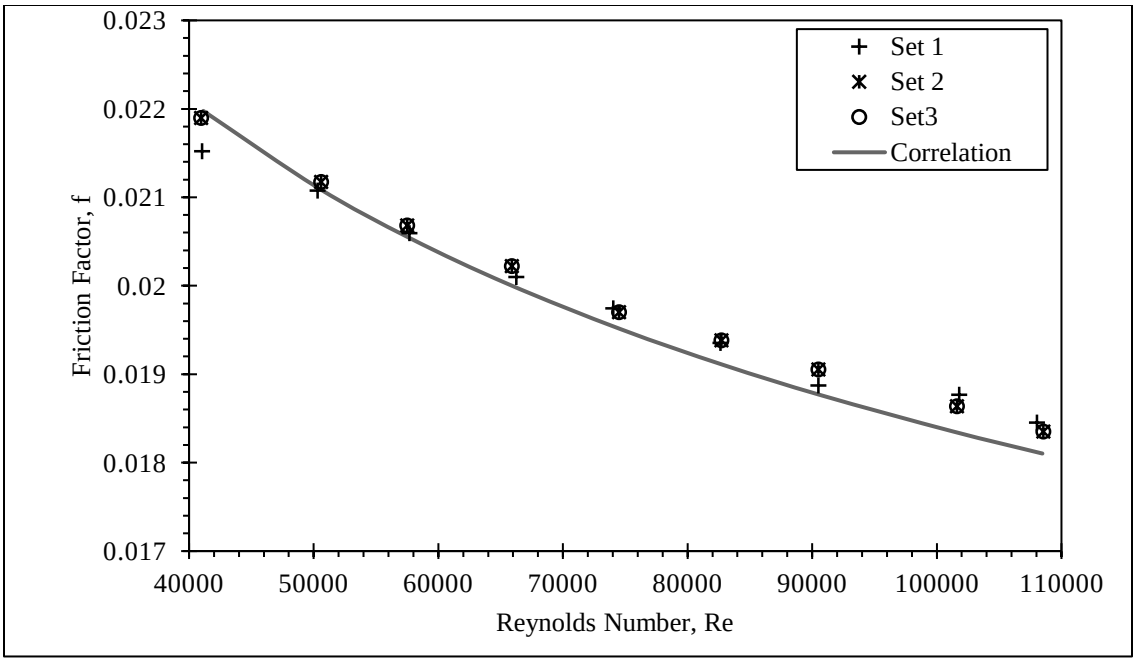

Figure 6.1 Comparison of Smooth Friction factor results from experiment with correlation

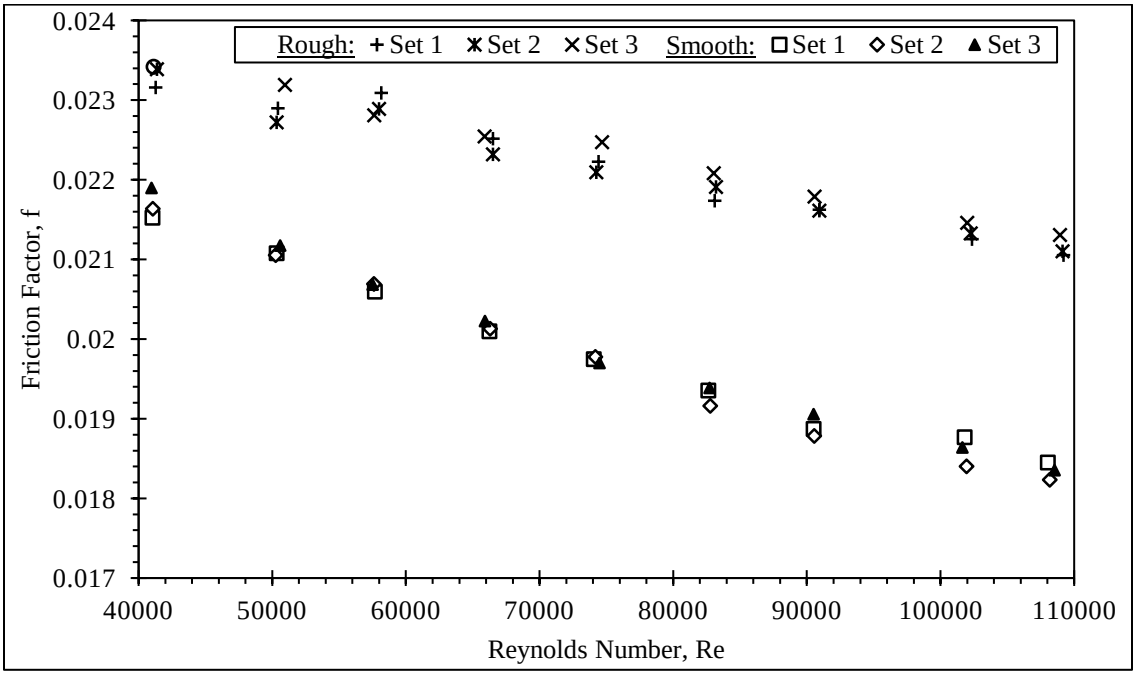

Figure 6.2 Comparison of experimental results of friction factor for SiC rod with the smooth rod.

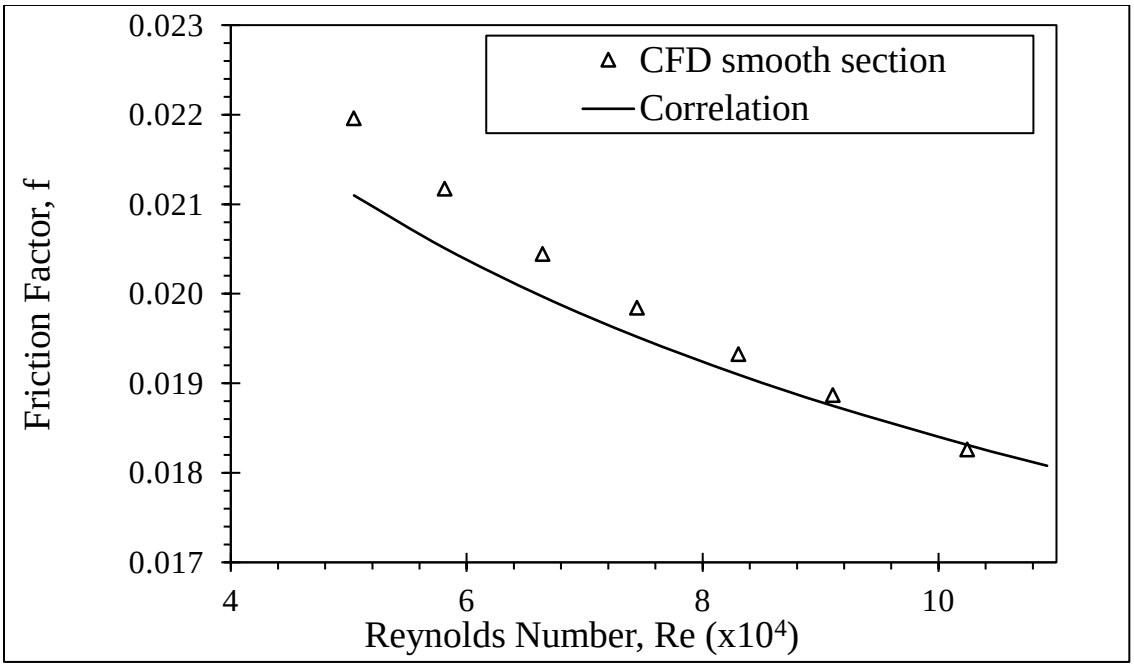

Figure 6.3 Comparison of friction factor for smooth rod from CFD analysis and Correlation

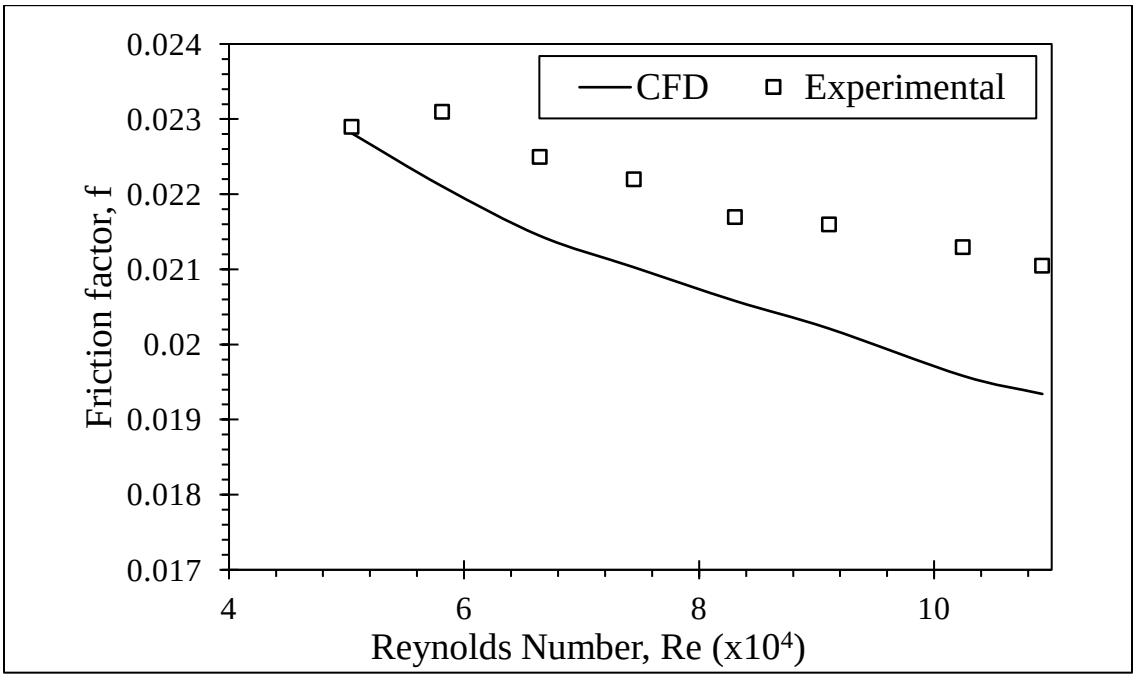

Figure 6.4 Comparison of friction factor obtained from Experiment and CFD analysis

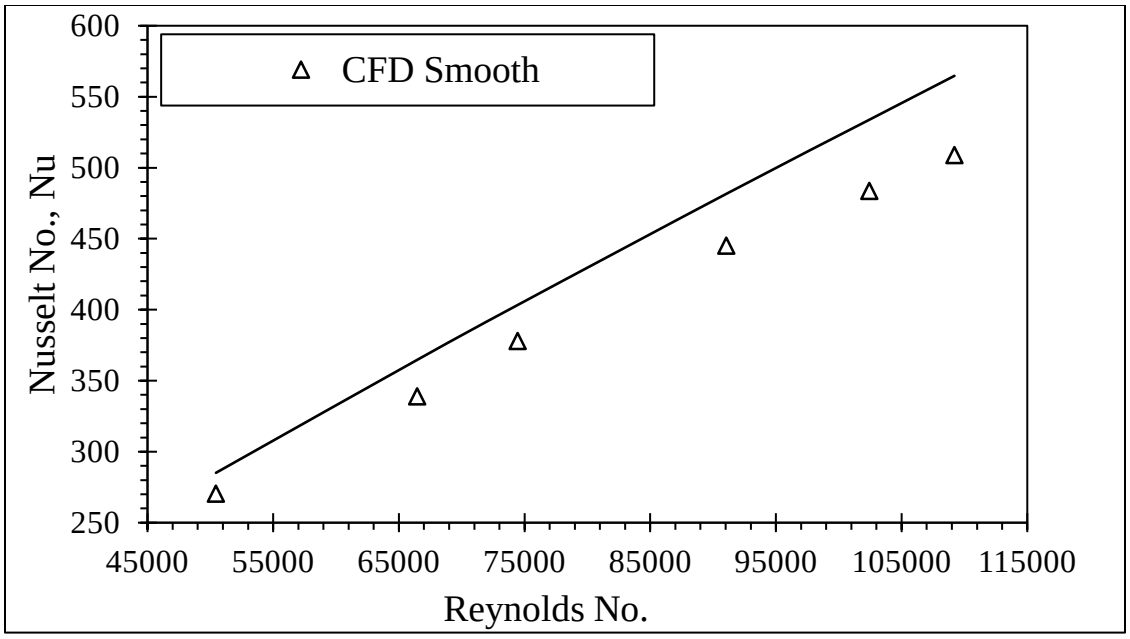

Figure 6.5 Comparison of Nusselt No. at the smooth section (y_1=0.737 m) from CFD analysis and Gnielinski Correlation.

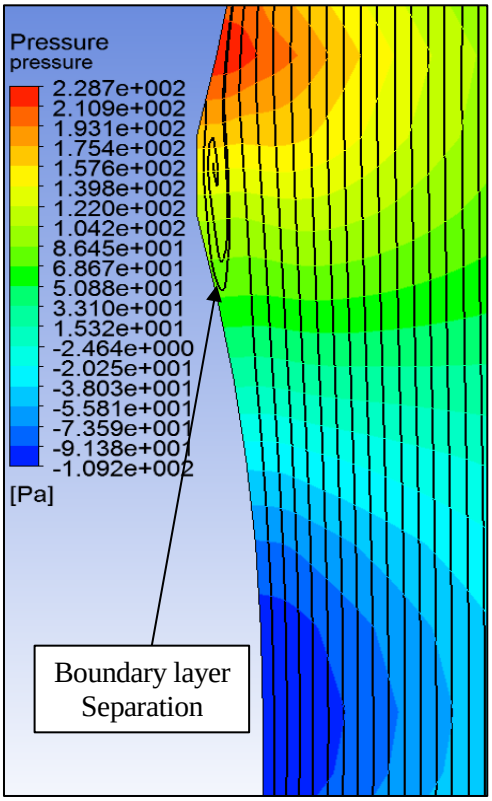

Figure 6.6 Pressure contours and streamlines around roughness structures (Re=102,436)

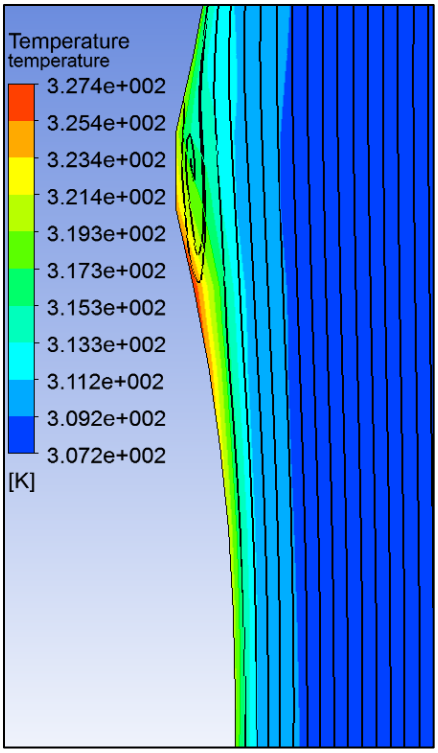

Figure 6.7 Temperature contours and streamlines around roughness structures (Re=102,436)

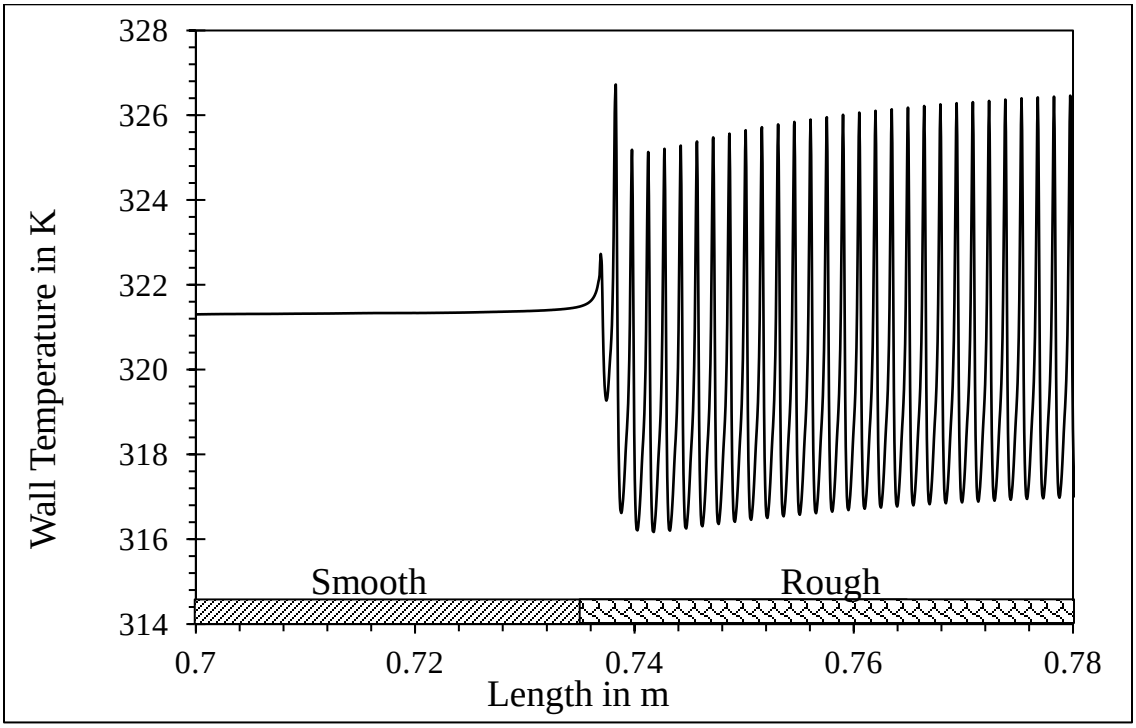

Figure 6.8 Wall Temperature variation T_{wr} along the rough wall

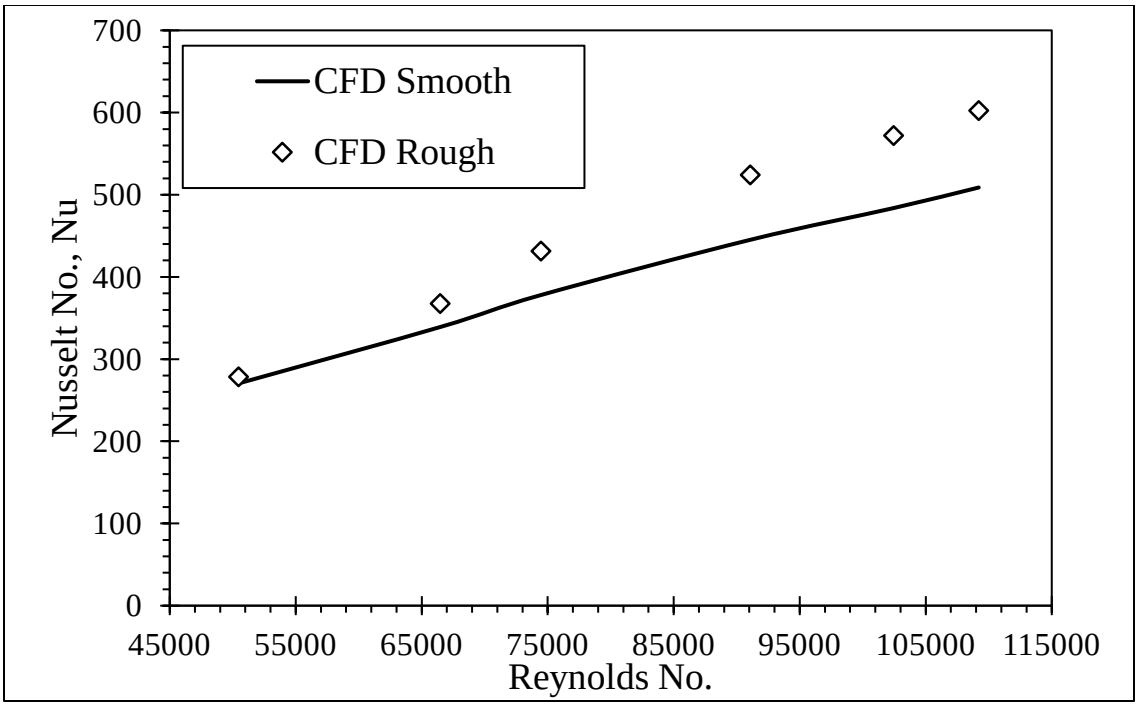

Figure 6.9 Comparison of Nusselt Number from CFD analysis for smooth and rough rods

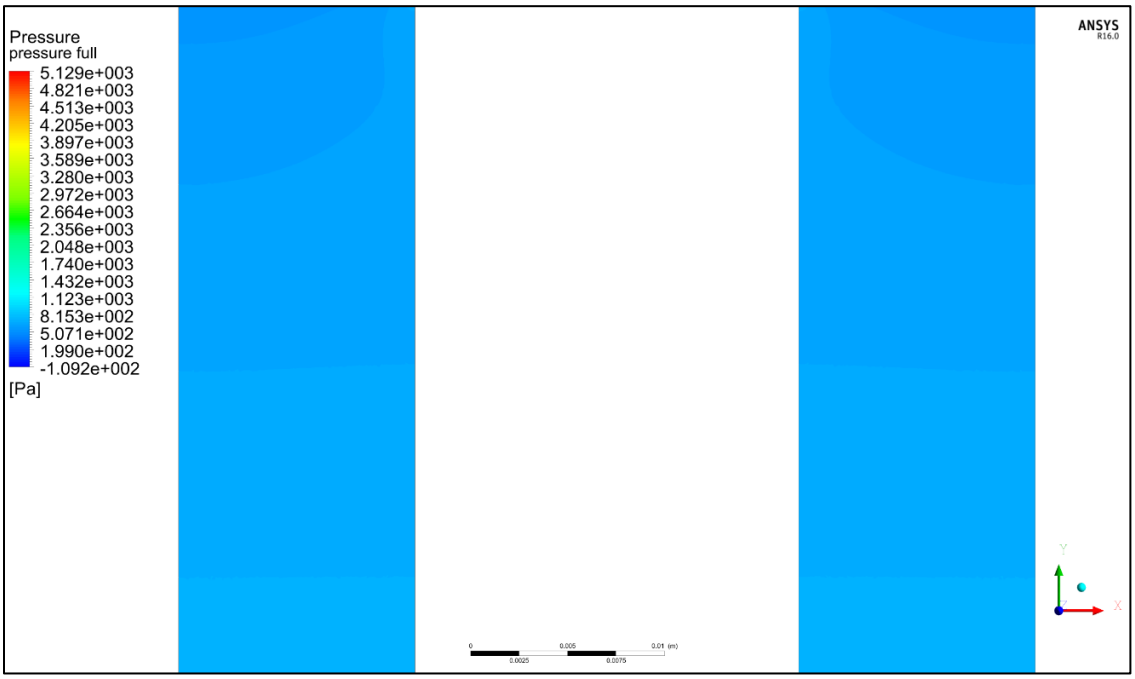

Figure 6.10 Contours of Pressure (Pa) in smooth section

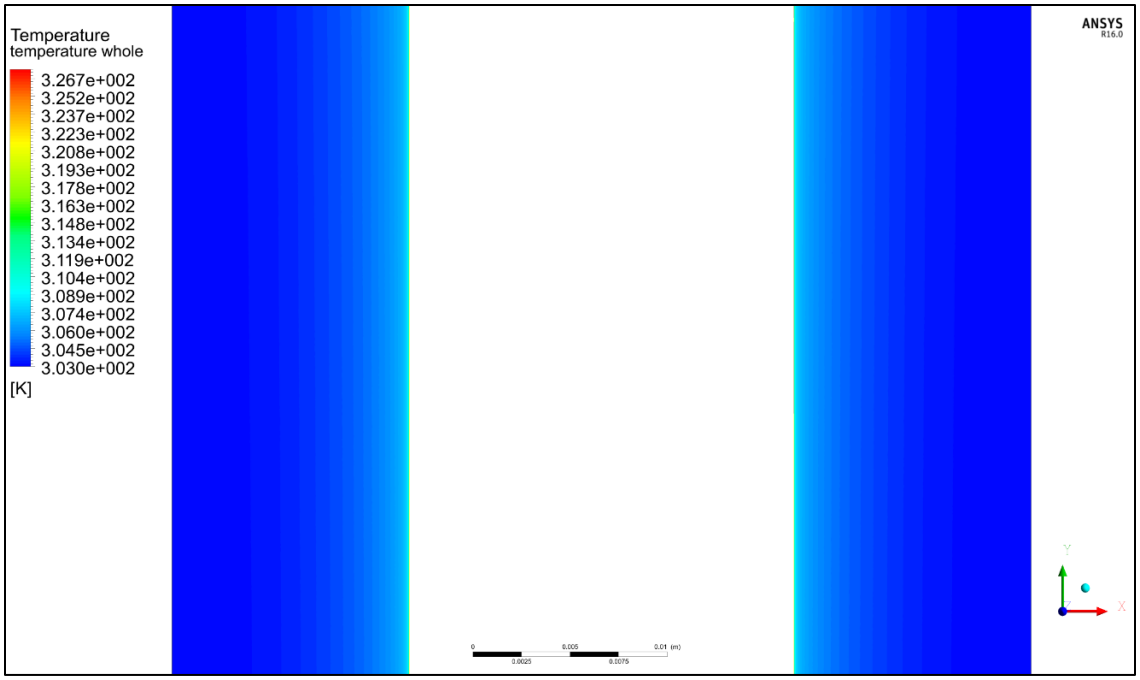

Figure 6.11 Contours of Temperature (K) in smooth section

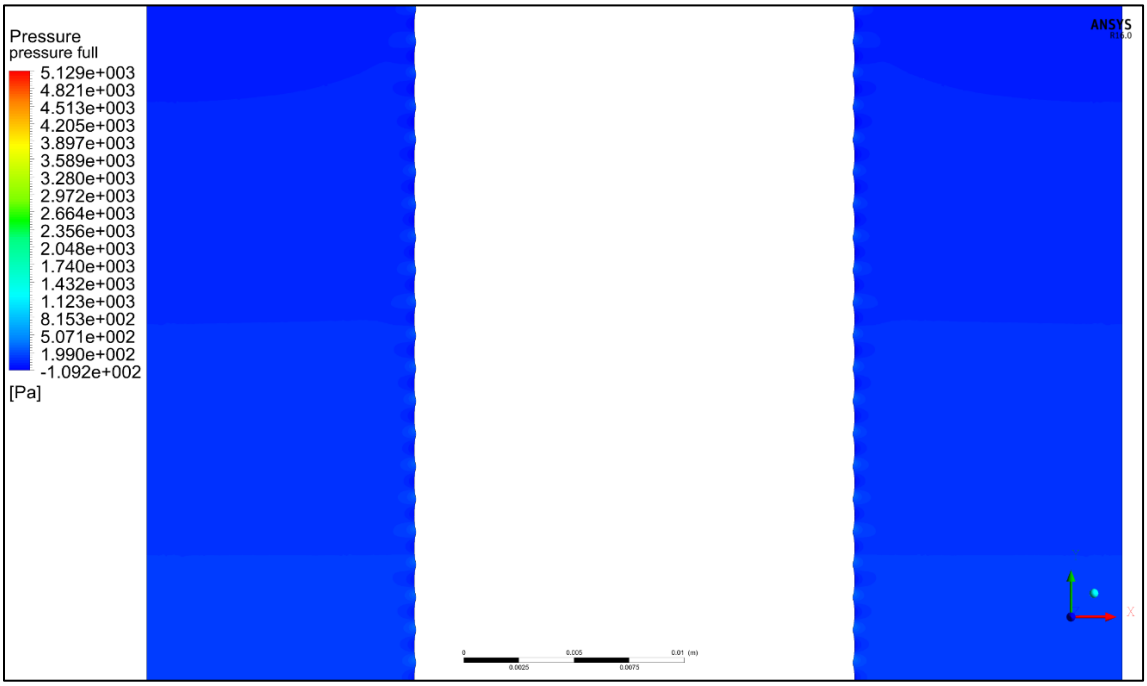

Figure 6.12 Contours of Pressure (Pa) in rough section

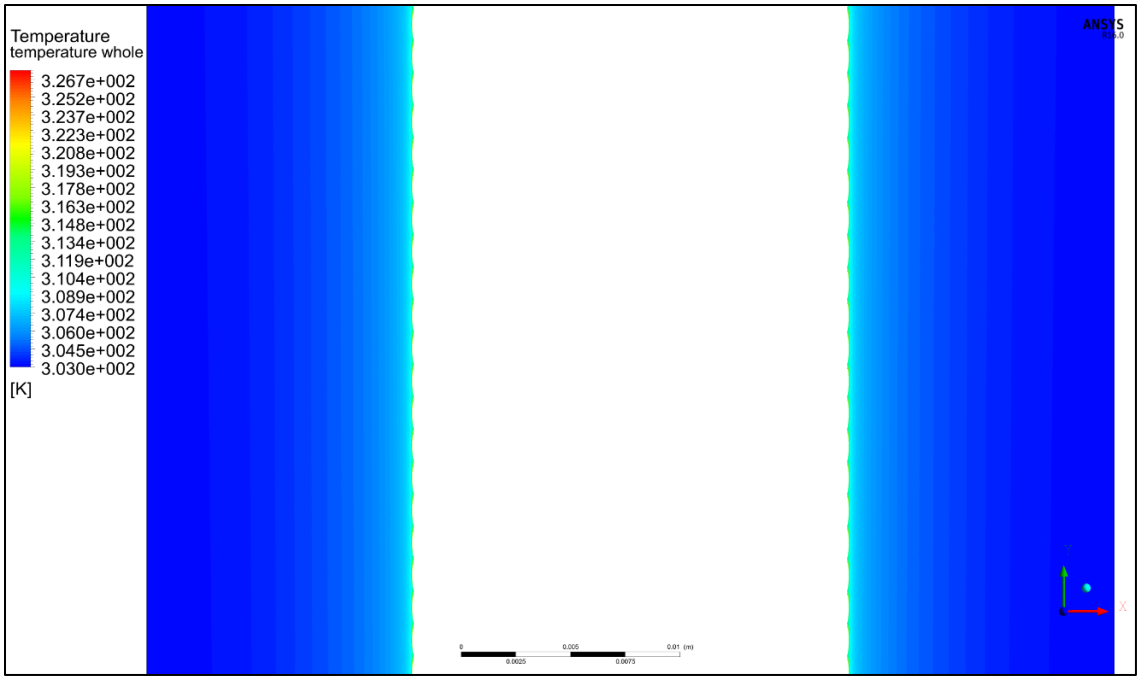

Figure 6.13 Contours of Temperature (K) in rough section

Table 6.1 Results for friction factor for smooth rods

Data Set	Flow Rate (m3/hr)	Um in m/s	Reynold's No.	Pressure drop (mmHg)	Pressure Drop (Pascal)	friction factor	friction factor (theoretical)
	4.831	1.345	41054	1.586	211.49	0.02152	0.02199
	5.923	1.650	50334	2.335	311.32	0.02108	0.02111
	6.789	1.891	57694	2.998	399.66	0.02059	0.02054
	7.798	2.172	66268	3.860	514.58	0.02010	0.01998
1	8.715	2.427	74061	4.736	631.43	0.01975	0.01954
	9.725	2.708	82644	5.781	770.68	0.01935	0.01912
	10.652	2.967	90522	6.762	901.54	0.01887	0.01877
	11.981	3.337	101816	8.508	1134.23	0.01877	0.01833
	12.713	3.541	108037	9.418	1255.61	0.01845	0.01812
	4.831	1.346	41075	1.596	212.83	0.02164	0.02198
	5.913	1.648	50275	2.327	310.24	0.02105	0.02111
	6.778	1.889	57629	3.005	400.61	0.02069	0.02054
	7.798	2.173	66302	3.869	515.86	0.02013	0.01998
2	8.726	2.431	74192	4.760	634.58	0.01977	0.01953
	9.735	2.713	82771	5.740	765.24	0.01916	0.01911
	10.652	2.968	90567	6.738	898.28	0.01878	0.01877
	11.991	3.341	101952	8.363	1115.01	0.01840	0.01833
	12.723	3.545	108176	9.330	1243.90	0.01823	0.01811
	4.821	1.343	40970	1.607	214.28	0.02190	0.02200
	5.954	1.658	50598	2.370	316.02	0.02117	0.02109
	6.768	1.885	57515	2.992	398.90	0.02068	0.02055
	7.757	2.160	65920	3.843	512.36	0.02022	0.02000
3	8.767	2.442	74503	4.782	637.53	0.01970	0.01952
	9.735	2.711	82729	5.802	773.47	0.01938	0.01911
	10.652	2.967	90522	6.828	910.31	0.01905	0.01877
	11.960	3.331	101638	8.420	1122.54	0.01864	0.01834
	12.774	3.558	108555	9.457	1260.80	0.01835	0.01810

Table 6.2 Friction Factor results with the rough SiC rod

Data Set	Flow Rate (m^3/hr)	Um (m/s)	Reynold's No.	Presure Drop (mmHg)	Pressure Drop (Pa)	friction factor
	4.842	1.343	41301	1.692	225.57	0.02316
	5.913	1.640	50437	2.495	332.59	0.02289
	6.82	1.891	58174	3.347	446.20	0.02309
	7.798	2.163	66516	4.267	568.81	0.02251
1	8.726	2.420	74431	5.274	703.11	0.02222
	9.745	2.703	83123	6.433	857.62	0.02174
	10.662	2.957	90945	7.661	1021.31	0.02162
	12.002	3.329	102375	9.542	1272.12	0.02125
	12.805	3.551	109225	10.759	1434.34	0.02105
	4.852	1.346	41387	1.716	228.74	0.02338
	5.903	1.637	50352	2.467	328.93	0.02272
	6.799	1.886	57994	3.298	439.63	0.02289
	7.798	2.163	66516	4.229	563.86	0.02232
2	8.705	2.414	74252	5.218	695.64	0.02209
	9.756	2.706	83217	6.498	866.34	0.02191
	10.662	2.957	90945	7.656	1020.68	0.02161
	11.991	3.326	102281	9.556	1273.99	0.02133
	12.795	3.548	109139	10.766	1435.26	0.02110
	4.821	1.337	41122	1.696	226.13	0.02342
	5.975	1.657	50966	2.580	343.95	0.02319
	6.758	1.874	57645	3.246	432.80	0.02281
	7.726	2.143	65902	4.193	559.06	0.02254
3	8.756	2.428	74687	5.369	715.78	0.02247
	9.735	2.700	83038	6.522	869.52	0.02208
	10.621	2.946	90595	7.660	1021.25	0.02179
	11.96	3.317	102017	9.565	1275.22	0.02146
	12.774	3.543	108960	10.835	1444.54	0.02131

Table 6.3 Friction Factor obtained from the CFD Analysis

Speed (m/s)	Reynold no	Friction factor		% change
		CFD	Correlation	
1.64	50449	0.02196	0.02110	-4.08
1.89	58139	0.02117	0.02051	-3.24
2.16	66445	0.02045	0.01997	-2.39
2.42	74443	0.01984	0.01952	-1.67
2.7	83056	0.01933	0.01910	-1.20
2.96	91054	0.01887	0.01875	-0.63
3.33	102436	0.01826	0.01831	0.28
3.55	109203	0.01797	0.01808	0.58

Table 6.4 Nusselt Number obtained from CFD analysis compared with Gnielinski Correlation

Speed (m/s)	Reynolds No.	Nusselt Number		
		CFD	Gnielinski Correlation	% Difference
1.64	50448.93883	270.3801	285.11523	5.1681362
2.16	66444.94382	338.9404	364.61341	7.0411498
2.42	74442.94632	377.8854	403.28234	6.2975507
2.96	91054.18227	445.1018	481.6051	7.5795182
3.33	102435.9551	483.732	533.80587	9.3805371
3.55	109203.4956	508.8259	564.70364	9.8950508

Table 6.5 Comparison of friction factor obtained from experiment and CFD analysis for the SiC Fuel rod

Speed	Reynold no	Friction factor		% change
		CFD	Experiment	
1.64	50449	0.02281	0.02290	0.39
1.89	58139	0.02211	0.02310	4.31
2.16	66445	0.02145	0.02250	4.68
2.42	74443	0.02103	0.02220	5.28
2.7	83056	0.02058	0.02170	5.16
2.96	91054	0.02021	0.02160	6.43
3.33	102436	0.01958	0.02130	8.06
3.55	109203	0.01934	0.02105	8.12

Table 6.6 Nusselt Number calculations for the SiC rod

Speed (m/s)	T_{b_1}	T_{b_2}	$T_{b_{avg}}$	T_{w_r}	h	Nu rough
1.64	305.291	305.775	305.533	338.57667	7036.416	278.4998
2.16	304.733	305.091	304.912	329.96415	9281.001	367.7831
2.42	304.536	304.536	304.536	325.90759	10879.35	431.309
2.96	304.254	304.254	304.254	321.8536	13211.04	524.0686
3.33	304.121	304.356	304.2385	320.36791	14415.22	572.0122
3.55	304.052	304.275	304.1635	319.48336	15176.96	602.3264

Table 6.7 % increasein Nusselt Number

Reynolds Number	CFD Analysis		% increase in Nusselt Number
	Smooth	Rough	
50449	270.38	278.50	3.00
66445	338.94	367.78	8.51
74443	377.89	431.31	14.14
91054	445.10	524.07	17.74
102436	483.73	572.01	18.25
109203	508.83	602.33	18.38

CHAPTER 7

CONCLUSION AND FUTURE RESEARCH

7.1 Conclusion

The objective of the research outlined in this thesis was to experimentally determine the friction factor of a simulated Silicon Carbide (SiC) nuclear fuel rod, with three dimensional surface roughnesses which was produced by vapor deposition and braiding of SiC fibres. The experimental results were compared with correlations and with experimental results from a smooth rod. The Single Heater Element Loop tester (SHELT) at USC was used to conduct the experimental testing. The experimental results were validated by checking with correlations, and then confirming repeatability of the results. The experimental results indicates that the roughness design on the SiC fuel rod will increase the flow resistance by 15% at the highest Reynolds number studied.

A Computational model was also established to study the friction factor and heat transfer enhancements for the SiC nuclear fuel rod. The roughness design on the SiC rod was modeled by using SolidWorks. The CFD model was established by using the ANSYS Fluent solver, which used Finite Difference Methods in order to solve the governing equations. The CFD model for the SiC fuel rod was validated by comparing with experimental results. The friction factor results obtained from the CFD results vary from the experimental results with a maximum deviation of 8%. This was considered to lie

within reasonable limits considering the inherent errors associated with the CAD design of the SiC roughness design. The thermal results obtained from the CFD analysis suggested that the roughness design will enhance heat transfer by at least 18.4% at the highest Reynolds number.

7.2 Future Research

In order to validate the thermal CFD model a experimental investigation with heat transfer should be conducted. This can be achieved by applying heat to the SiC fuel rod using the Power Supply already available in the SHELT Loop. The rod can be heated by either using of cartridge heater or by using resistive heating techniques as was done in previous investigations [13], [14].

REFERENCES

[1] L. Meyer, A. Bastron, J. Hofmeister, and T. Schulenberg, “Enhancement of Heat Transfer in Fuel Assemblies of High Performance Light Water Reactors,” *J. Nucl. Sci. Technol.*, vol. 44, no. 3, pp. 270–276, 2007.

[2] S. C. Johnson, H. Patts, and D. E. Schuler, “Mechanical Behavior of SiC f / SiC CMC Tubes Relative to Nuclear Fuel Cladding,” *Proc. ICAPP 2014*, pp. 2287–2295, 2014.

[3] T. S. Ravigururajan and A. E. Bergles, “Development and verification of general correlations for pressure drop and heat transfer in single-phase turbulent flow in enhanced tubes,” *Exp. Therm. Fluid Sci.*, vol. 13, no. 1, pp. 55–70, 1996.

[4] H. L. Heinisch, L. R. Greenwood, W. J. Weber, and R. E. Williford, “Displacement damage cross sections for neutron-irradiated silicon carbide,” *J. Nucl. Mater.*, vol. 307–311, no. Part 2, pp. 895–899, 2002.

[5] D. Carpenter, G. Kohse, and M. Kazimi, “Modeling of silicon carbide duplex cladding designs for high burnup light water reactor fuel,” in *International congress on advances in nuclear power plants*, 2007.

[6] D. M. Carpenter, “An assessment of silicon carbide as a cladding material for light water reactors,” Massachusetts Institute of Technology, 2014.

[7] J. Nikuradse, “Laws of flow in rough pipes,” in *National Advisory Committee for Aeronautics*, 1950.

[8] M. E. Steinke and S. G. Kandlikar, “Review of single-phase heat transfer

enhancement techniques for application in microchannels, minichannels and microdevices," *Int. J. Heat Technol.*, vol. 22, pp. 3–11, 2004.

[9] R. J. Firth and L. Meyer, "A comparison of the heat transfer and friction factor performance of four different types of artificially roughened surface," *Int. J. Heat Mass Transf.*, vol. 26, no. 2, pp. 175–183, 1983.

[10] X. W. Li, J. A. Meng, and Z. X. Li, "Roughness enhanced mechanism for turbulent convective heat transfer," *Int. J. Heat Mass Transf.*, vol. 54, no. 9–10, pp. 1775–1781, 2011.

[11] D. N. Ryu, D. H. Choi, and V. C. Patel, "Analysis of turbulent flow in channels roughened by two-dimensional ribs and three-dimensional blocks. Part I: Resistance," *Int. J. Heat Fluid Flow*, vol. 28, pp. 1098–1111, 2007.

[12] D. N. Ryu, D. H. Choi, and V. C. Patel, "Analysis of turbulent flow in channels roughened by two-dimensional ribs and three-dimensional blocks. Part II: Heat Transfer," *Int. J. Heat Fluid Flow*, vol. 28, pp. 1112–1124, 2007.

[13] L. Carrilho, "Experimental and Computational study of roughened surface for PWR rod bundles," University of South Carolina, 2012.

[14] U. Najeeb, "Heat Transfer Characteristics of Three-Dimensional Surface Roughness in Nuclear Fuel Rod Bundles," in *International Mechanical Engineering Congress & Exposition*, 2013.

[15] D. F. Dippery and R. H. Sabersky, "Heat and Momentum Transfer in Smooth and Rough Tubes at Various Prandtl Numbers," *Int. J. Heat Mass Transf.*, vol. 6, pp. 328–353, 1963.

[16] F. P. Incropera, D. P. DeWitt, T. L. Bergman, and A. S. Lavine, *Fundamentals of*

Heat and Mass Transfer, 6th Editio. 2006.

[17] F. M. White, *Viscous fluid flow*, 2nd Editio. 1991.

[18] A. 16.0, "FLUENT Manual," .

[19] S. E. Haaland, "Simple and Explicitly Formulas for the Friction Factor in Turbulent Pipe Flow," *J. Fluids Eng.*, vol. 105, pp. 89–90, 1983.

[20] F. R. Menter, "Zonal two equation k- ω turbulence models for aerodynamic flows," *AIAA Pap.*, vol. 2906, 1993.

[21] F. R. Menter, M. L. Suc, and M. Library, "Two-equation eddy-viscosity turbulence models for engineering applications," *AIAA J.*, vol. 32, pp. 1598–1605, 1994.

[22] F. R. Menter, "Influence of freestream values on k-w turbulence model predictions," *AIAA J.*, vol. 30, pp. 1657–1659, 1992.

[23] V. Gnielinski, "New equations for heat and mass transfer in the turbulent flow in pipes and channels," *Int. Chem. Eng.*, vol. 75, pp. 359–368, 1976.